Transcriptomic changes in retinal ganglion cell types associated with the disruption of cholinergic retinal waves

Rachana Deven Somaiya[a,1], Matthew A. Po[b,1], Marla B. Feller[a,2], Karthik Shekhar[b,c,d,2]

[a]Department of Neuroscience & Helen Wills Neuroscience Institute, University of California, Berkeley, Berkeley, CA 94720, USA.
[b]Department of Chemical and Biomolecular Engineering, University of California, Berkeley, Berkeley, CA 94720, USA.
[c]Helen Wills Neuroscience Institute, University of California, Berkeley, Berkeley, CA 94720, USA.
[d]Faculty Scientist, Biological Systems and Engineering Division, Lawrence Berkeley National Laboratory, Berkeley, CA 94720, USA

[1]R.D.S. and M.A.P. contributed equally to this work.
[2]To whom correspondence may be addressed. Email: mfeller@berkeley.edu or kshekhar@berkeley.edu

Abstract

In the early stages of retinal development, a form of correlated activity known as retinal waves causes periodic depolarizations of immature retinal ganglion cells (RGCs). Retinal waves are crucial for refining visual maps in the brain's retinofugal targets and for the development of retinal circuits underlying feature detection, such as direction selectivity. Yet, how waves alter gene expression in immature RGCs is poorly understood, particularly at the level of the many distinct types of RGCs that underlie the retina's ability to encode diverse visual features. We performed single-cell RNA sequencing on RGCs isolated at the end of the first postnatal week from wild-type (WT) mice and β2KO mice, which lack the β2 subunit of the nicotinic acetylcholine receptor, leading to the disruption of cholinergic retinal waves. Statistical comparisons of RGC transcriptomes between the two conditions reveal a weak impact of retinal waves on RGC diversity, indicating that retinal waves do not influence the molecular programs that instruct RGC differentiation and maturation. Although wave-dependent gene expression changes are modest in the global sense, we identified ~238 genes that are significantly altered in select subsets of RGC types. We focused on one gene, *Kcnk9*, which encodes the two-pore domain leak channel potassium channel TASK3. *Kcnk9*, which is highly enriched in αRGCs, was strongly downregulated in β2KO. We validated this result using *in situ* hybridization and performed whole-cell recording to demonstrate a significant decrease in the leak conductance in β2KO RGCs. Our dataset provides a useful resource for identifying potential targets of spontaneous activity-dependent regulation of neurodevelopment in the retina.

Introduction

The visual system is a classical model for exploring how electrical activity patterns in immature neurons shape the development and refinement of neural circuits. In the retina, the outpost of the visual system within the eye, roles of activity-independent and activity-dependent development of neural circuits have been extensively studied (1). Retinal development begins in the embryo, with the birth and differentiation of retinal ganglion cells (RGCs). As the sole output neurons of the retina, RGCs comprise more than 40 distinct types in mice that can be classified using morphological, physiological, connectomic, and molecular attributes (2–7). In adult mice, RGCs of a given type form highly precise connections with other types of presynaptic neurons in the inner retina, which renders most individual RGC types selectively responsive to a small subset of visual features such as orientation, directional motion, and edges (8, 9). The diverse feature detection capabilities of RGCs form the basis of vision, making the differentiation of these neurons and their assembly into highly precise synaptic circuits a central feature of early visual system development.

The time course of RGC development and the environment in which they develop is well described. RGCs become postmitotic between embryonic day 11 (E11) and E17 and begin to extend axons that pass through the optic nerve and innervate diverse retinorecipient targets (10–12). The elaboration of dendritic structure occurs during the first two weeks of postnatal life, with RGCs forming synapses with amacrine cells and, later, bipolar cells in the retina's inner plexiform layer. As they differentiate into discrete types during this period, immature RGCs exhibit spontaneous wave-like activity, also known as retinal waves, which precede photoreceptor-driven responses (13–15).

Retinal waves span a protracted period during early development, starting on E17 and persisting through eye-opening on postnatal day 12 (P12) (16). During the embryonic period and first postnatal week, waves are generated via cholinergic signaling networks orchestrated by starburst amacrine cells (SACs) that release acetylcholine onto neighboring SACs and RGCs (17–19). In the second postnatal week, the circuits that mediate waves transition to early glutamatergic circuits, driven by spontaneous depolarization in bipolar cells (20). These waves travel throughout the visual system and are the primary source of activity in the dorsal lateral geniculate nucleus (dLGN) (21, 22), superior colliculus (SC), and primary visual cortex prior to the onset of vision (23, 24).

Numerous studies have implicated the role of spontaneous activity induced by cholinergic waves in the refinement of retinal projections to the brain, including the retinotopic refinement of RGC axons and segregation of eye-specific RGC terminals in the dLGN and SC as well as the functional development of visual response properties (21, 25–29). Importantly, different RGC types project to different brain regions and these innervation patterns are differentially impacted by activity (28, 30). For example, disruption of the normal wave propagation patterns disrupts the alignment of direction-selective responses in the SC along the axes defined by optic flow (31).

Cholinergic waves have also been implicated in the development of RGC response properties, though this is less explored across cell types. Several studies have shown that cholinergic signaling impacts the development of dendrites in subsets of RGCs (32–36). Recently, we showed that cholinergic waves are important for establishing the functional circuitry corresponding to a subset of RGCs that selectively respond to horizontal directional motion in the mouse retina (37). Hence, the impact of waves on retinal circuit development does not necessarily lead to large neurite rearrangements but rather may be due to changes in factors that dictate the synapse-specific wiring that is critical for functional circuit development. This impact on circuit development is likely to occur in an RGC type-dependent manner.

To address how neural activity impacts the development of the different RGC types, we used single-cell RNA sequencing (scRNAseq) to compare RGC transcriptomes between wild-type (WT) and mice lacking the β2 subunit of neuronal nicotinic receptor. Genetic removal of the β2 subunit of the nicotinic acetylcholine receptor inhibits cholinergic signaling, thereby disrupting retinal waves between E16 and P7 (18, 32, 38, 39). This mouse model, henceforth called β2KO, has been used widely to study the developmental roles of spontaneous activity-induced by cholinergic waves. Our analysis focused on several key aspects: the effects of these waves on RGC type diversification, the global transcriptomic shifts across all RGC types, and type-specific changes to identify RGC types with higher sensitivity to wave disruption. To contextualize the magnitude of these transcriptomic changes, we compared differences between P7 WT and P7 β2KO mice with the developmental transcriptional shifts in WT RGCs from P5 to P7. One candidate activity-regulated gene was further validated using *in situ* hybridization and functional assays. Our approach provides a comprehensive investigation of transcriptional regulation by cholinergic retinal waves and generates a valuable resource for identifying potential activity-dependent genes during a critical developmental window.

Results

Disrupting cholinergic retinal waves does not impact RGC diversification or composition

To assess the impact of cholinergic retinal waves on the RGC transcriptome, we used droplet-based scRNAseq (10X Chromium v3) to profile retinas from WT and β2KO mice at P7 (**Fig. 1A**). We chose P7 as it represents the final phase of wave reduction and precedes the onset of premature glutamatergic waves in β2KO (32). As RGCs comprise fewer than 1% of all retinal cells, we enriched them using CD90-conjugated magnetic beads, following previously established protocols (**Methods**; 40). We obtained 47,361 transcriptomes passing quality metrics, which includes the number of detected genes per cell (>700) and transcripts per cell (>5,000) detected, and a low proportion of mitochondrial transcripts per cell (< 10%). We classified these cells into major retinal classes based on the selective expression of marker genes (**Fig. 1B**). RGCs could be identified based on their high expression of the gene *Slc17a6*, which encodes the glutamate transporter VGLUT2; *Rbpms*, which encodes an RNA-binding protein; and the transcription factor encoding genes *Pou4f1-3* (**Fig. 1B**). Expression levels of *Chrnb2,* the gene encoding the β2 subunit of nicotinic acetylcholine receptor, were significantly lower in β2KO RGCs compared to WT RGCs, but was not zero (**Fig. 1B**). A closer examination

revealed that the low basal level of expression in β2KO was due to reads mapping to another gene, *Adar*, whose 3' end overlaps with the 3' end of *Chrnb2* (**Fig. S1**). The remaining cell classes comprised amacrine cells, bipolar cells, Müller glia, endothelial cells, and microglia (**Fig. 1C**). Overall, ~99% of cells in the WT dataset (n=27,274 cells) and ~93% in the β2KO dataset (n=16,684 cells) were identified as high-quality RGCs (>1800 genes/cell and >5,000 transcripts/cell), indicating a successful enrichment. The rest of the paper focuses exclusively on RGCs.

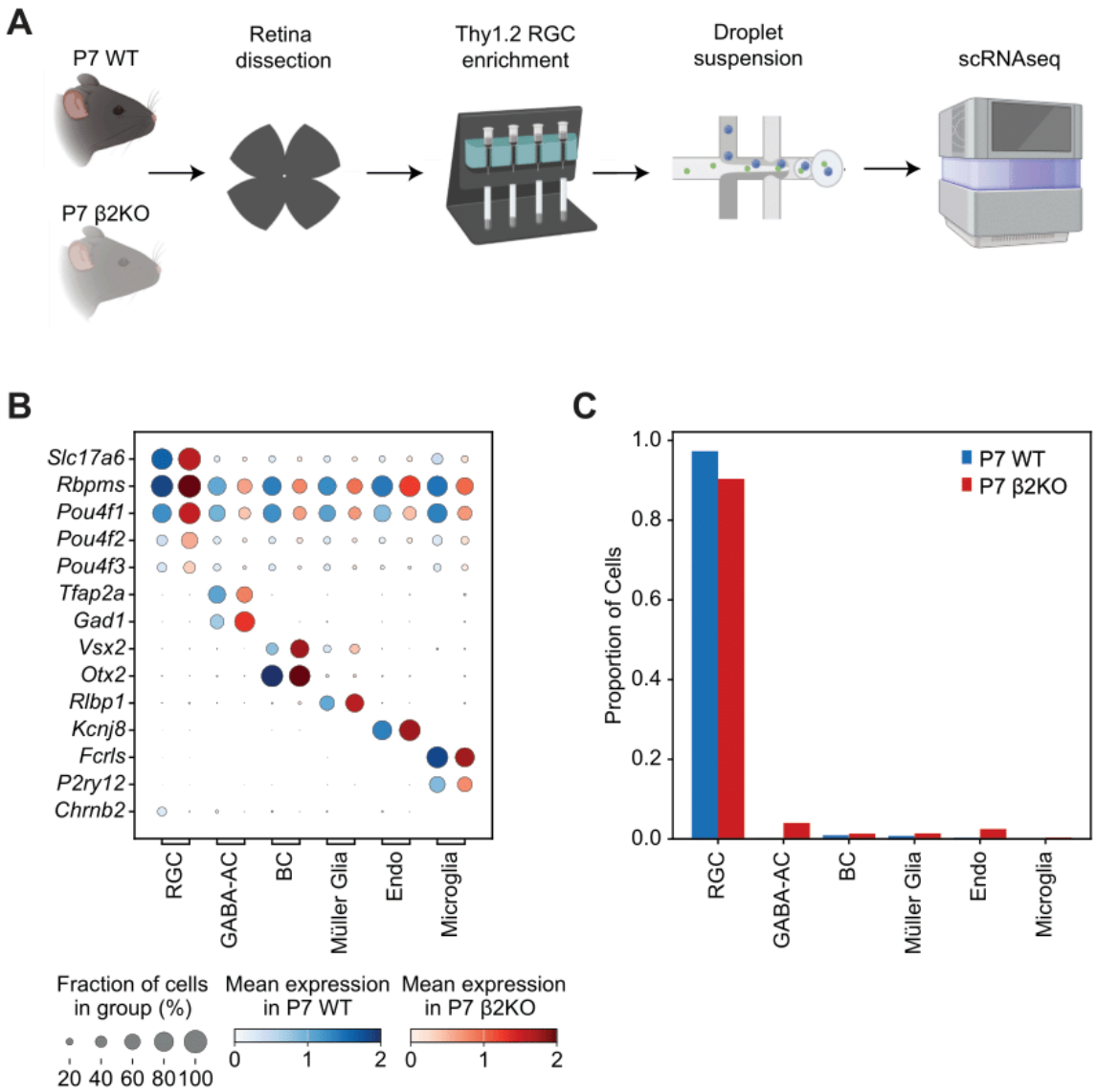

Figure 1. Study overview and enrichment of RGCs. (A) Overview of RGC enrichment and scRNAseq profiling from WT and β2KO mice. **(B)** Dotplot showing expression patterns of well-known markers (rows) in retinal cell classes (columns) within either condition. For each cell class, the expression levels in the WT and β2KO correspond to blue and red dots, respectively. The size of each dot corresponds to the percentage of cells in each class expressing the marker, and the color indicates the normalized expression level (see legend, bottom). **(C)** Barplot showing the relative proportion of major retinal cell

groups (x-axis) in either dataset. BC, bipolar cells; GABA-AC, GABAergic amacrine cells; Endo, Endothelial cells. Note that we did not detect appreciable numbers of photoreceptors and horizontal cells, two prominent retinal cell classes.

To begin, we applied standard dimensionality reduction and clustering approaches to identify transcriptomically distinct clusters of RGCs in both WT and β2KO samples (**Methods; Fig. S2**). To relate transcriptomic clusters to RGC types defined previously, we trained a supervised classifier on a published atlas of adult (P56) RGCs (Tran et al., 2019) and applied this classifier to each P7 RGC (**Figs. 2A, B; Methods**). Based on an ensemble voting procedure, the classifier assigns each P7 RGC a P56-type label (C1-C45) and an associated measure of confidence. Using this procedure, most P7 RGCs (>91 % in WT and >96% in β2KO) could be mapped to an adult type with high confidence (**Methods**). Cells mapping to the same RGC type also co-clustered in the reduced dimensional space (**Fig. 2B**). Because several molecularly defined types have been mapped onto morphologically and functionally defined types in recent studies (3, 5, 7), we were able to identify cells corresponding to well-known groups of types, such as alpha (α) RGCs (41), ON-OFF and ON direction-selective RGCs (DSGCs), intrinsically photosensitive (ip) RGCs, and FoxP2 RGCs (42). The P7 datasets contained all 45 molecularly defined RGC types.

We verified these classifications *post hoc* by comparing cell type-specific gene expression patterns across the three datasets: P7 WT, P7 β2KO, and P56 WT. In previous works, we have shown that the 45 RGC types can be grouped into eight “subclasses” based on the selective expression of transcription factor (TF) encoding genes (40, 43). The three datasets showed consistent expression patterns of these subclass-defining TFs (**Fig. 2C**), as well as of other TFs and recognition molecules (**Fig. S3**). Although some types varied in composition between P7 WT and P7 β2KO, and between P7 WT and P56 WT, we found that the overall rank order of the relative frequency was highly correlated across the datasets (Pearson $R > 0.8$, $p < 10^{-15}$) (**Fig. 2D-E**). Notably, the variations in type-frequencies between P7 WT and P7 β2KO were comparable in magnitude to those observed between biological replicates within the same condition (**Fig. 2F**), suggesting that these differences may not be biologically relevant. Taken together, the presence of all types in WT and β2KO, and the absence of any apparent differences in frequency composition suggest that retinal waves do not impact the diversification of RGCs. However, the disruption of retinal waves may still lead to altered gene expression without affecting the differentiation of types, which we now explore.

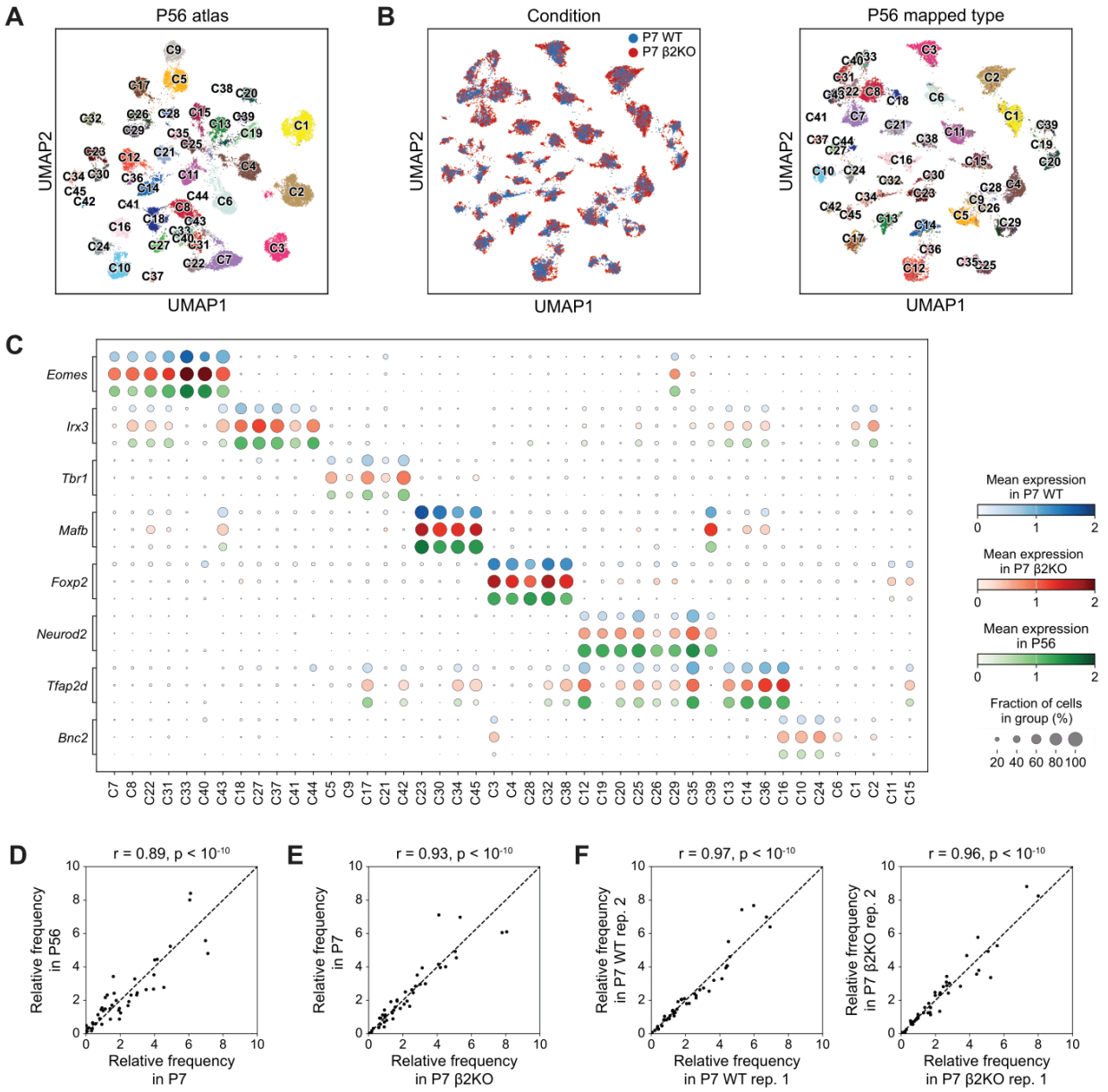

Figure 2. Disruption of waves minimally impacts RGC diversification. (A) Uniform Manifold Approximation and Projection (UMAP) embedding of adult (P56) RGCs from (7) colored by molecularly defined types C1-C45. **Table S1** relates type IDs to commonly used type names. **(B)** Integrated UMAPs of cells from WT and β2KO RGCs at P7, colored by condition (left) and inferred type label (right) using a supervised classifier trained on P56 data. **(C)** Dotplot showing the expression patterns of subclass-specific transcription factors (row blocks) in each RGC type (columns). Within each row block, the three rows correspond to P7 WT (blue), P7 β2KO (red), and P56 WT (green). **(D)** Scatter plot comparing the relative frequency, *i.e.* cells in a cluster, between P56 WT and P7 WT. Each dot represents one RGC type. **(E)** Same as D, for P7 WT and P7 β2KO. **(F)** Same as D, for two replicates of P7 WT (left) and two replicates of P7 β2KO (right).

Wave-dependent transcriptomic changes are modest globally but significant at the type-specific level

We next sought to characterize transcriptomic changes associated with the disruption of waves. To assess the magnitude of these changes, we first computed differentially expressed genes (DEGs) along the course of normal development by comparing WT RGCs at P7 with WT RGCs at P56 and at P5. The P5 data was obtained from our previous study (40) using an older droplet-based technology (44). P5 and P7 lie in the period over which cholinergic retinal waves occur. RGCs elaborate dendrites and make synapses with bipolar cells and amacrine cells in the inner plexiform layer before the detection of the first light responses (~P10). The retina is mature by P56. Integration of the published P5 and P56 RGC datasets with P7 WT and P7 β2KO datasets revealed that cells mixed well and separated by their adult type labels, even though the type labels were not used explicitly to guide the integrated clustering procedure (**Fig. 3A**).

We first assessed global transcriptomic changes (*i.e.*, without regard to cell type identity) across each pair of datasets, beginning with developmental changes. At a threshold of log2-fold change with log2FC > 1 and adjusted p-value $p_{adj} < 0.05$ (Wilcoxon rank-sum test), there were 3880 differentially expressed genes (DEGs) between P5 and P56 WT and 3560 DEGs between P7 and P56 WT. 2233 genes were common among the two sets with a statistically significant overlap (hypergeometric test, $p < 10^{-10}$), highlighting that, as expected, P5 and P7 are more similar to each other than each of them is to P56 (**Fig. 3B, left**). We also found 1882 DEGs between P5 and P7, suggesting considerable transcriptional regulation between these two temporally proximal time points (**Fig. 3B, right**). By contrast, there were only 21 genes that were globally differentially regulated between P7 WT and P7 β2KO. This wide disparity implies that wave-dependent changes are modest even when compared to changes that occur during two days of normal development, as evidenced by the greater spread along the y-axis in the right scatterplot of **Fig. 3B**. On the other hand, we identified no DEGs between biological replicates within P7 WT or P7 β2KO, suggesting that these modest changes may be biologically meaningful (**Fig. 3C**).

We hypothesized that the disruption of cholinergic waves may impact RGC types non-uniformly, such that an impacted gene is dysregulated in only a few RGC types. Combined with several unaffected types, these changes may be washed out in global comparisons. Accordingly, within each type, we computed DEGs that were wave-dependent or developmentally regulated. Though developmental changes still dominate, we identified many type-specific, wave-dependent DEGs that did not appear in the global comparisons (**Fig. 3D**). Overall, we found 238 genes that were significantly upregulated or downregulated (log2FC > 1, $p_{adj} < 0.05$) in individual types. On average, each gene was regulated in 3-8 types, and each type had 18 ± 9 DEGs. To understand what biological processes are represented amongst these type-specific, wave-dependent genes, we performed a Gene Ontology (GO) enrichment analysis on the DEGs (45–47). The top terms enriched among both the upregulated and downregulated genes included processes related to cell-cell adhesion, and synaptic and neuropeptide signaling, indicating that there may be subtle, type-specific changes in gene expression that potentially influence the development of visual circuitry (**Fig. 3E**). Contributing to the enrichment of these processes were several genes that encode potassium channels and subunits of

neurotransmitter (e.g. GABA, glutamate) receptors, which are highlighted in **Fig. 3F** and **Fig. S4**.

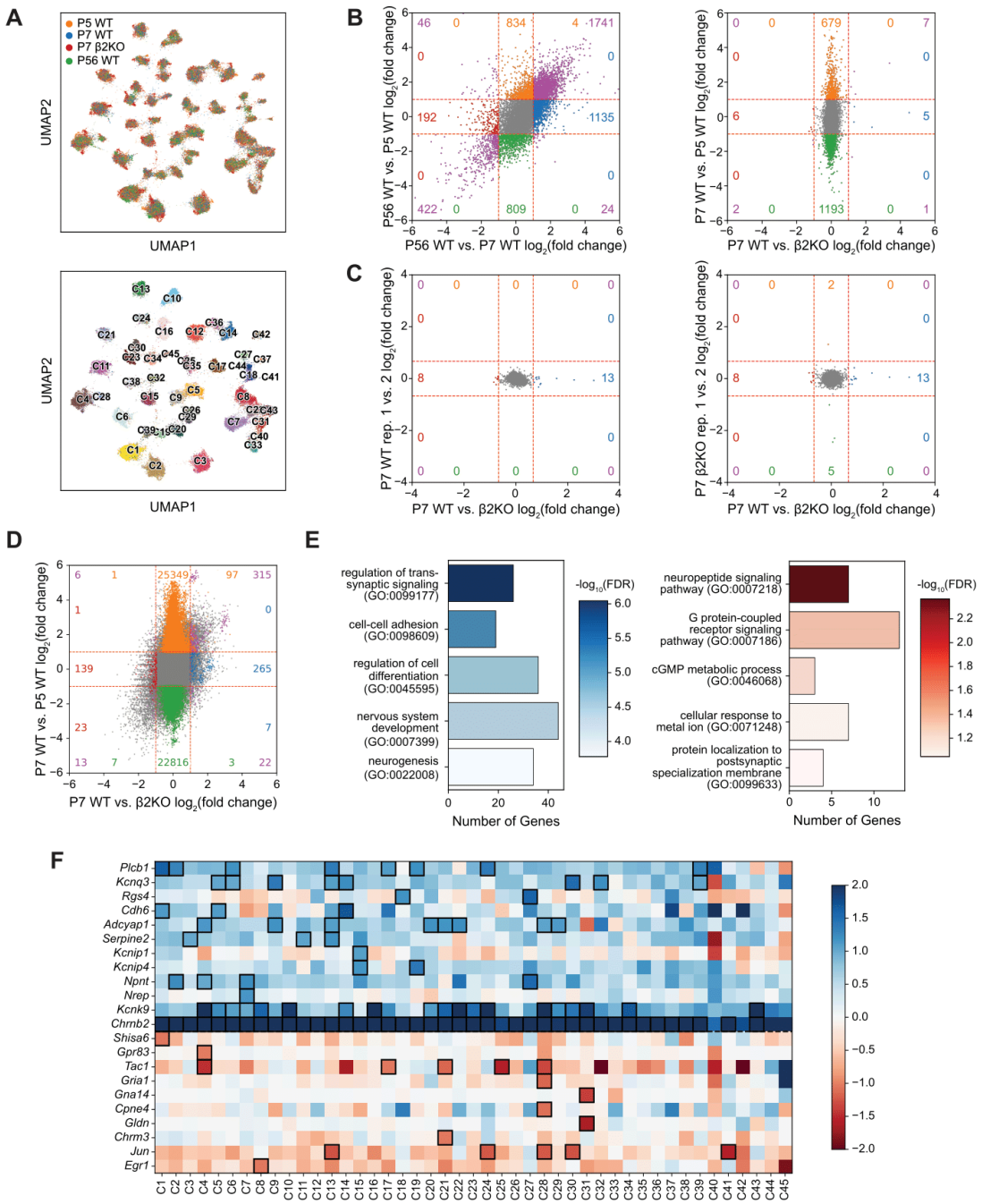

Figure 3. Global and type-specific wave-dependent transcriptomic changes. (A) Integrated UMAP of cells from P5 WT, P7 WT, P7 β2KO, and P56 WT colored by the dataset of origin (top) and mapped adult type (bottom). **(B)** Comparisons of log2-fold changes (log2FC) in global gene expression across datasets. Left panel compares WT datasets: P56 vs. P5 (y-axis) with P56 vs. P7 (x-axis). Right panel compares P7 WT vs. P5 WT (y-axis) with P7 WT vs. P7 β2KO (x-axis). Colored dots represent significantly up/downregulated genes (log2FC > 1, Wilcoxon rank-sum test adjusted p-value < 0.05). Each color

represents significant up/downregulation in one comparison, and purple represents genes that are significantly up/downregulated across both comparisons. For comparisons W vs. X on the x-axis and Y vs. Z on the y-axis, genes upregulated in W vs. X are blue, genes downregulated in W vs. X are red, genes upregulated in Y vs. Z are orange, genes downregulated in Y vs. Z are green, and genes that fall into any two of these categories are purple. Colored numbers represent the count of genes falling in each category. **(C)** Comparisons of log2FC in global gene expression between the two P7 conditions and between biological replicates. Left panel compares P7 WT replicate 1 vs. replicate 2 (y-axis) with P7 WT vs. P7 β2KO (x-axis). Right panel compares P7 β2KO replicate 1 vs. replicate 2 (y-axis) with P7 WT vs. P7 β2KO (x-axis). Colors as in (B). **(D)** Comparisons of log2FC in type-specific gene expression between P7 WT vs. P5 WT (y-axis) and P56 vs. P5 (y-axis) with P56 vs. P5 (x-axis). Each dot corresponds to a gene-type combination (e.g. *Chrnb2* in C33). Colors as in (B). **(E)** GO terms overrepresented in the genes significantly downregulated (left, blue) and upregulated (right, red) in β2KO. **(F)** WT vs. β2KO log2-fold changes in expression of example genes contributing to the GO terms shown in E. Black boxes indicate significant up/downregulation of a gene in a type (log2FC > 1, Wilcoxon rank-sum test $p_{adj} < 0.05$).

Wave-dependent RGC subclass-specific regulation

Our previous work has shown that the β2KO has a dramatic reduction in direction-selective responses of horizontal-motion preferring DSGCs (37). Mouse DSGCs can be classified into two main subclasses, ON-OFF and ON, via their mode of light responses. ON-OFF DSGCs can be further divided into four types (dorsal (D), ventral (V), nasal (N), and temporal (T)) and ON DSGCs into three (D, V, and N) based on their directional preference (48–52). In the β2KO, we saw a reduction in the direction-selective responses of N- and T-ON-OFF DSGCs as well as N-ON DSGCs, while all vertical DSGCs retained their tuning. Importantly, we should note that in the β2KO, N-ON-OFF DSGCs still existed, but had only lost their tuning properties.

To assess the differential impact of wave disruption on the different DSGC types, we first had to identify the cell types transcriptomically at P7. At P56, three clusters of ON-OFF DSGCs have been previously reported: C12 as N-ON-OFF DSGCs, C16 as a mix of D- and V-ON-OFF DSGCs, and recent studies identifying C24 as T-ON-OFF DSGCs (3, 5). Through supervised analysis, C16 can be subclassified into dorsal and ventral types based on expression of *Calb1* and *Calb2* (D: high *Calb1*/low *Calb2*, V: high *Calb2*/low *Calb1*). C10 in the adult atlas has recently been mapped to ON-DSGCs in both mouse (3, 5, 53), and primate (54, 55), but further subclustering of C10 into the D, V and N varieties was unsuccessful in the adult data (**Fig. 4A**).

By contrast, the D, V, and N types among ON DSGCs could be molecularly distinguished at earlier stages (**Fig. 4A**). We found that immature RGCs mapping to C10 in the adult formed three clusters during development, which mapped 1:1 between P5 and P7. **Figure 4B** summarizes the molecular taxonomy of all DSGC types at the three ages. Moreover, these ON DSGC gene signatures at P5 and P7 were consistent with a recent study which analyzed molecular diversity of ON DSGCs by applying Smart-seq2 to FACS-enriched RGCs obtained from a knockin transgenic mouse line that selectively labels ON DSGCs (56). Finally, results suggest that while ON-OFF marker distinctions persist from P5 into adulthood, those associated with ON DSGCs are lost during maturation (**Fig. 4B**). As all our datasets employ droplet-based

scRNAseq, these results also argue against the possibility that our inability to resolve ON DSGC diversity in adult mice is due to technical sampling limitations.

With the DSGC classifications in hand, we examined whether horizontal DSGCs are more susceptible to waves than vertical ones. To quantify the magnitude of wave disruption, we use the ratio of wave-dependent DE gene counts to developmental DE gene counts as a metric for susceptibility to waves. A comparison of DSGC types reveals minor variations in this ratio from type to type, with these differences being very small in magnitude, suggesting that transcriptomically no DSGC type was more susceptible to wave disruption (**Fig. 4C**).

We then expanded this analysis to other RGC subclasses, including *Foxp2*-RGCs, ipRGCs, and αRGCs. We calculated wave-dependent/developmental DE count ratios for all RGC types, then grouped these ratios by subclass.While subtle differences were observed, there was no significant variation in mean ratios across subclasses (one-way ANOVA, $p = 0.13$) (**Fig. 4D**). Though the magnitude of wave-dependent changes does not seem to differ significantly across subclasses, it may be the case that waves regulate similar gene expression changes in certain RGC subclasses. To investigate this, we computed pairwise correlations in gene log2-FCs across all RGC types (**Fig. 4E**). This revealed stronger correlations in wave-dependent expression changes between types within certain subclasses, namely in ON-OFF DSGCs and W3-RGCs, suggesting subclass-specific and correlated wave-dependent gene regulation.

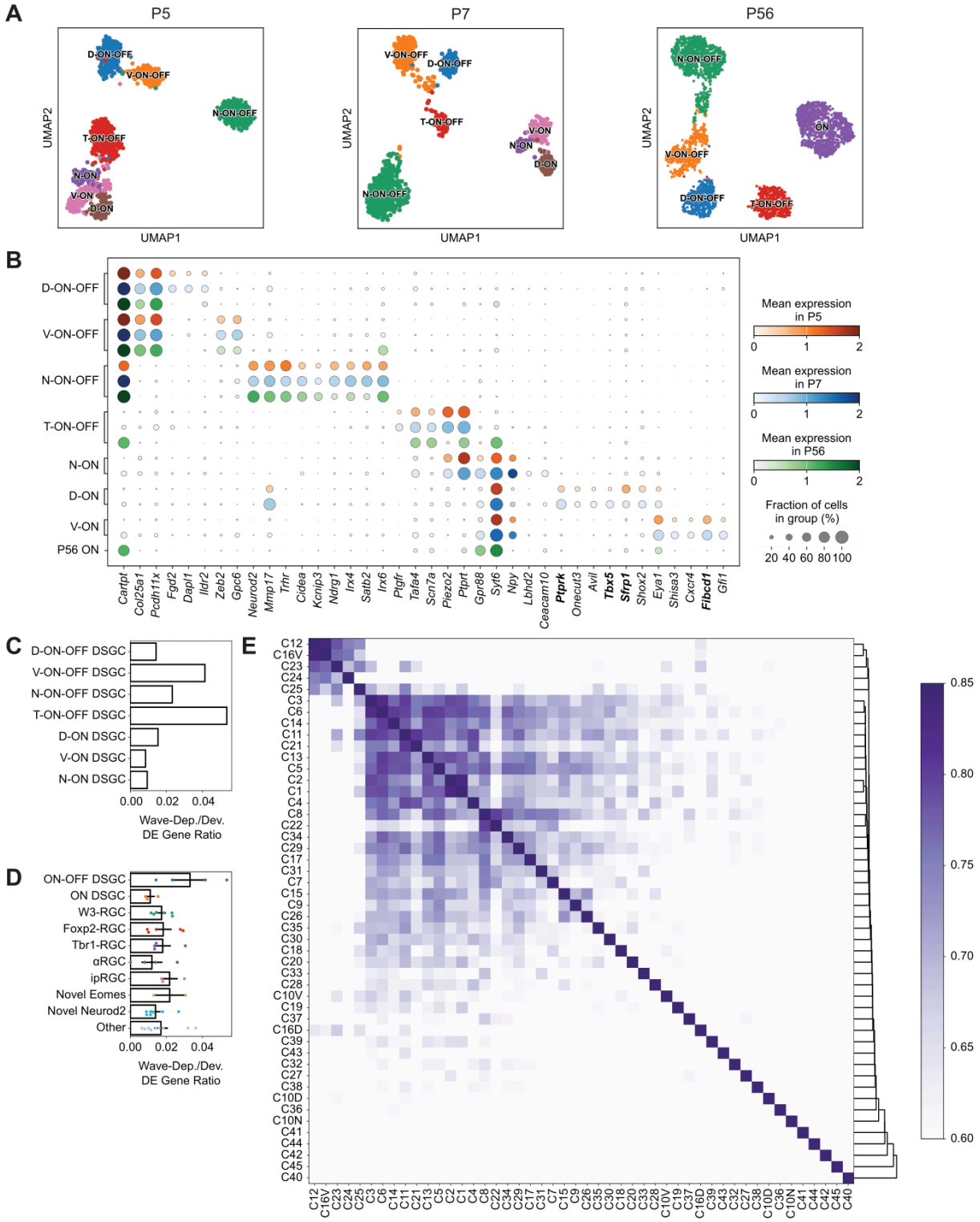

Figure 4. Classification of DSGCs and analysis of subclass-specific, wave-dependent regulation. **(A)** UMAP representations of DSGCs at P5, P7, and P56, colored by DSGC type. **(B)** Expression of marker genes for each DSGC type across the age conditions. Only P5 and P7 are represented for individual ON-DSGC types, with the bottom row showing expression in the unclustered ON-DSGC group at P56. Genes in bold correspond to markers for ON-DSGCs during development. **(C)** Ratios of

wave-dependent (P7 WT vs. P7 β2KO) to developmental (P7 vs. P5) DE gene counts per DSGC type. **(D)** Ratios of wave-dependent (P7 WT vs. P7 β2KO) to developmental (P7 vs. P5) DE gene counts per RGC subclass, with points representing individual types. Bars lengths represent mean ± SEM. **(E)** Pairwise correlations in gene log2FC between RGC types, ordered based on hierarchical clustering. Darker colors represent stronger correlations. **Table S1** relates cluster IDs (7) to commonly used type names. DSGC clusters split here (C16 and C10) are appended with the letter corresponding to their preferred direction (e.g. C16V represents V-ON-OFF DSGCs).

Expression of a leak potassium channel is modulated by waves.

To assess the overall impact of wave-dependent gene regulation on RGCs, we focused on *Kcnk9*, a gene downregulated in many β2KO RGC types (**Fig 5A**). *Kcnk9* encodes TASK-3, a two-pore-domain leak potassium channel, which has been shown to contribute to neuronal excitability in αRGCs (57). Therefore, we focused on αRGCs in this study. *Kcnk9* mRNA expression was downregulated in all four types of αRGCs, though statistical significance could only be established for one type due to sampling limitations (**Fig S5**). We used *in situ* hybridization (ISH) to validate the downregulation of *Kcnk9* in β2KO RGCs. Combined with immunohistochemistry (IHC) for SMI32, an αRGC marker, these experiments also showed a robust decrease in *Kcnk9* expression within SMI32$^+$ αRGCs (**Fig 5B-D**).

To assess the impact on leak channel-associated conductance in αRGCs, we conducted voltage-clamp recordings. αRGCs were identified in a flat-mounted retina as RGCs with soma diameters of >15 μm. To isolate the leak channel-associated conductance, these recordings were done in the presence of tetrodotoxin (TTX, 500nM) to block voltage-gated sodium channels and 4-aminopyridine (4-AP, 5 mM) to block voltage-gated potassium channels (**Figs. 5E, F**). β2KO αRGCs showed significantly reduced leak channel-associated conductance compared to WT (**Fig. 5G**), consistent with reduced expression of TASK3. These data show that transcriptomic changes in *Kcnk9* expression in β2KO alter outwardly rectifying potassium currents and suggest that disrupting stage 2 retinal waves likely increases the intrinsic excitability of αRGCs, a potential form of homeostatic regulation.

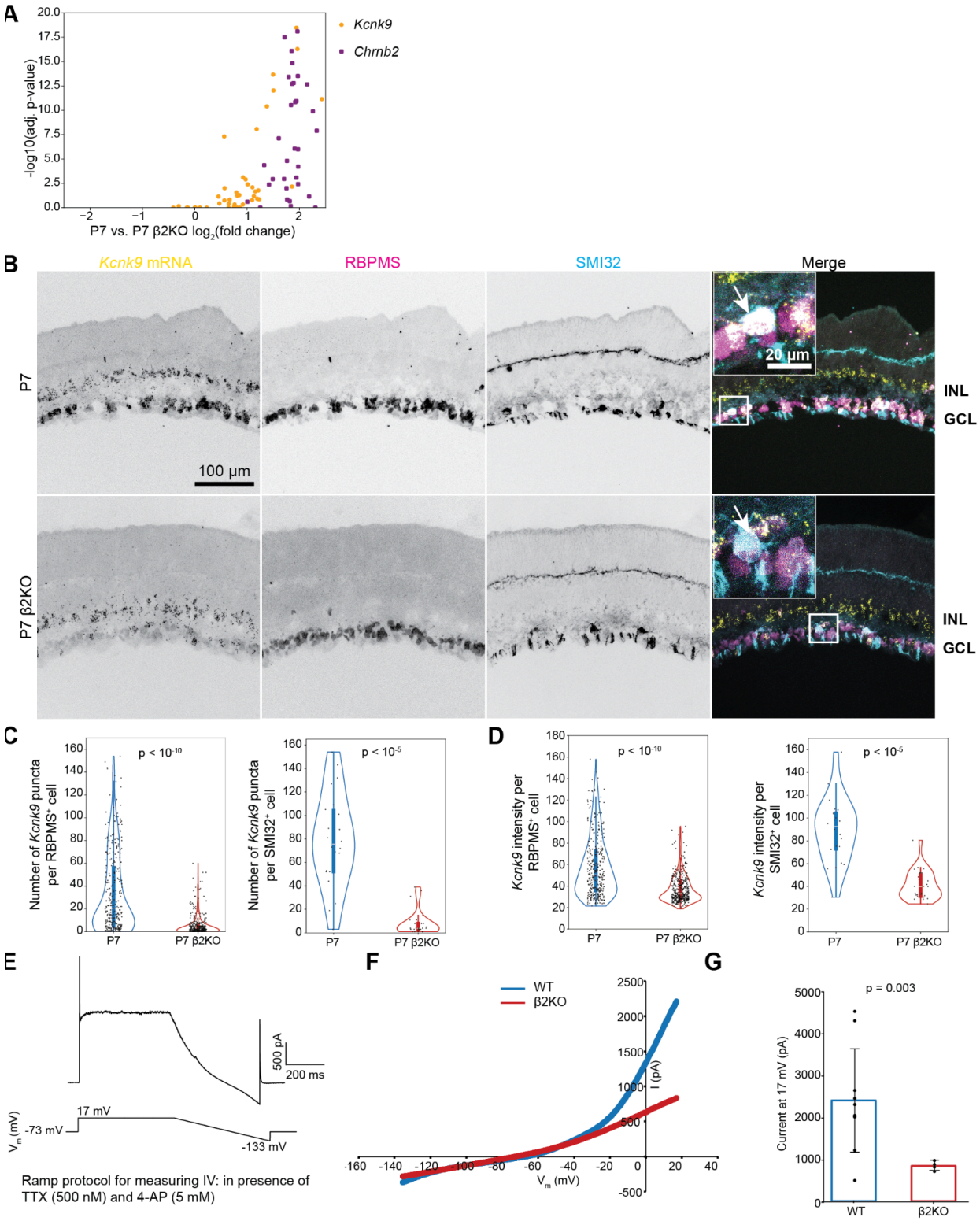

Figure 5. Expression of leak channel TASK3 impacted by retinal waves and its functional impact in RGCs. (A) Volcano plot depicting type-level log2-fold changes and Wilcoxon rank-sum test adjusted p-values for *Chrnb2* (purple squares) and *Kcnk9* (orange circles). Each dot corresponds to an RGC type. **(B)** ISH for *Kcnk9* mRNA (yellow) on P7 WT and β2KO retinal slices. IHC staining to identify RGCs

labeled with RBPMS (magenta) and αRGCs labeled with SMI32 (cyan). Inserts depict high-magnification images where arrows indicate high (in P7 WT) or low (P7 β2KO) expression of *Kcnk9* in RBPMS$^+$SMI32$^+$ αRGCs. **(C, D)** Quantification for number of *Kcnk9* puncta and fluorescence intensity in RBPMS$^+$ cells (left) and SMI32$^+$ cells (right) in P7 WT and β2KO. Each data point represents value from an individual cell. $p < 10^{-10}$ for RBPMS$^+$ cells and $p < 10^{-5}$ for SMI32$^+$ cells (Mann-Whitney U Test). **(E)** Voltage-clamp ramp protocol used previously to characterize TASK3 (57) (bottom) and example response trace from αRGC (top). **(F)** Example current-voltage curve of αRGCs from P7 WT (blue) and P8 β2KO (red) mice, P7-P12. **(G)** Summary data based on current recorded at Vhold = 17 mV in αRGCs WT (n=10) and β2KO (n=4), P7-P12. Each data point represents the value from an individual cell. Error bars = standard deviation, p value determined by Welch's two-sample t-test.

Discussion

Using scRNAseq profiles of developing RGCs, we found that the disruption of retinal waves in β2KO mice did not impact cell type specification, indicating that differentiation of RGCs occurs independently of spontaneous activity. This allowed us to assess how waves impacted gene expression in RGCs as a whole as well as within individual RGC types. Although wave-dependent changes in the transcriptome were more subtle than developmental changes, we identified several genes that show RGC-type-specific regulation in their expression by cholinergic retinal waves. Among these, we focused on *Kcnk9*, which encodes the leak potassium channel TASK3 and was significantly downregulated in αRGCs and a few other RGC types. Interestingly, despite profound effects on response properties, β2KO produced minimal transcriptional changes in ON-OFF DSGCs, suggesting that activity-dependent influence on retinal circuits does not prominently manifest at the transcriptomic level.

The absence of cholinergic waves does not impact RGC differentiation

The conventional view of neuronal differentiation into diverse cell types is that it occurs largely independent of neuronal activity (58). However, several studies have revealed a role of spontaneous activity in neuronal diversification within various areas of the central nervous system. For example, in the *Xenopus* spinal cord, spontaneous high-frequency calcium activity initiates a signaling cascade that drives unspecialized neurons to acquire a GABAergic identity (59, 60). Similarly, varied firing patterns of spontaneous activity among olfactory sensory neurons have been shown to induce the expression of unique axon-sorting molecules, conferring distinct identities to these neurons and enabling their axons to segregate into specific glomeruli within the mouse olfactory bulb (61–65). Comparable roles for spontaneous activity have been observed in the cochlea, where activity during the pre-hearing phase regulates the specification of type I spiral ganglion neurons (66, 67). Even in later stages of development, there are examples of sensory activity contributing to cell type specification. Olfaction-driven sensory activity is crucial for the differentiation of specific interneuron populations within the mouse olfactory bulb (68, 69), while visual experience during the critical period plays a pivotal role in the development and spatial patterning of glutamatergic cell types in the upper layers of the mouse primary visual cortex (70).

In the retina, RGCs diversify gradually, with the full complement of 45 molecularly distinct types emerging only by the end of the first postnatal week (P5) (40). Notably, this diversification is unaffected by activity changes induced by visual deprivation (43). Here, we extend these findings to show that even early postnatal spontaneous retinal activity, occurring prior to vision-driven activity, does not impact the diversification of RGC types. These results suggest that RGC diversification is likely guided by an intrinsic, activity-independent mechanism, aligning with the classical view of neuronal differentiation.

Comparisons with other transcriptomic studies on visual system development

Understanding the molecular impact of retinal waves on visual circuitry is crucial to elucidating how they impact visual system development. Recent studies have explored this impact at various levels of the visual system. For example, significant wave-dependent transcriptomic changes have been observed in cells of the visual cortex (24) and the superior colliculus (71). Additionally, waves have been implicated in the regulation of genes that govern axonal remodeling at retinorecipient targets (28). Through our study, we sought to reveal the molecular impact of waves on the retina itself.

The wave-dependent transcriptional changes we observe in the retina are very modest compared to those observed in other areas of the visual system. This suggests that, while waves originate in the retina, their molecular impact lies primarily within downstream structures of the visual pathway. We found this result to be surprising, as our previous study has suggested a role for waves in functionality tied to specific RGC types (37). Nevertheless, this helps to paint a more complete picture of the role that retinal waves play in the broader visual system.

While changes to the RGC transcriptome are modest, they are not entirely absent. Wave-dependent differences in expression became more evident when we inspected at the level of RGC types. Several of the genes regulated by wave activity are known to be involved in development, indicating that waves may be playing a subtle role in the regulation of these processes at the level of cell types. Further, we found that in many cell types, waves regulate the expression of *Kcnk9*, which encodes the leak potassium channel TASK3. The role of TASK3 in modulating intrinsic excitability suggests a connection between retinal waves and the intrinsic excitability of RGCs.

Disruption of cholinergic waves leads to modest transcriptomic changes across DSGC subtypes

Previously, we showed that disrupting cholinergic retinal waves impairs horizontal direction selectivity in the retina but preserves vertical-motion preference of DSGCs (37) This aligns with other studies showing that retinal waves specifically influence the horizontal optokinetic reflex ((72). These results suggest that horizontal and vertical motion-preferring direction-selective circuits in the retina develop through distinct signaling pathways, some of which are regulated by activity.

The emergence of direction-selective circuits coincides with robust wave activity. The direction preference of DSGCs is based on their wiring with SACs. Presynaptic SAC processes provide greater synaptic inhibition to postsynaptic DSGCs during null direction motion. This is a result of two features: 1) individual processes of SACs are more strongly depolarized by outward motion and 2) more synapse formation between SAC processes that are oriented antiparallel to the null direction of DSGCs (73, 74). Paired recording between SACs and DSGCs has revealed that the asymmetric inhibitory synaptogenesis occurs between P9 to P11 in the mouse retina (75–78). During this period, vertical- and horizontal-motion preferring DSGCs exhibit distinct transcriptome with numerous DEGs shown to be critical for synapse development in other contexts (76).

In this study, we investigated whether any of the differentially expressed genes in DSGCs are regulated by neural activity and whether the transcriptomes of horizontal-motion preferring DSGCs are particularly susceptible to wave disruption. Conducting this analysis during development provided an advantage, as unlike in adults, distinct ON-DSGC subtypes form separate transcriptomic clusters in the developing retina (**Fig 4B**). Surprisingly, intersectional analysis revealed that none of these DEGs were wave regulated (**Fig. 4C**), suggesting that spontaneous activity-mediated DSGC wiring does not occur by modulating cell-intrinsic genetic programs. While this result may also reflect the limited resolution of single-cell sequencing, which captures only about 15% of the cell's transcriptome (79), it is also possible that retinal waves exerts their influence through post-transcriptional or translational processes in DSGCs (80). Such activity-dependent mechanisms have been observed in the hippocampus, where activity regulates the local translation of matrix metalloproteinase-9, a protein crucial for regulating spine morphology in neurons (81). Similar activity-dependent local translation may act in DSGC synapses, potentially influencing their wiring with SACs. The development of newer technologies, such as isolating specific synapses using mouse transgenic lines or performing proximity protein labeling followed by mass spectrometry, could help investigate this possibility (82, 83).

Acknowledgments and funding sources
Some images were made using BioRender. We thank Dr. Justin Choi from the QB3/Functional Genomics Lab for assistance with scRNAseq. Funding sources include NIH EY028625 (KS), Society of Hellman Fellows (KS), McKnight foundation (KS), Glaucoma Research Foundation (KS), Weill Neurohub (RDS), NIH EY013528 (MF), and NIH EY019498 (MF).

References

1. W. A. Stevens-Sostre, M. Hoon, Cellular and Molecular Mechanisms Regulating Retinal Synapse Development. *Annu. Rev. Vis. Sci.* **10**, 377–402 (2024).
2. T. Baden, *et al.*, The functional diversity of retinal ganglion cells in the mouse. *Nature* **529**, 345–350 (2016).
3. J. Goetz, *et al.*, Unified classification of mouse retinal ganglion cells using function, morphology, and gene expression. *Cell Rep.* **40**, 111040 (2022).
4. J. A. Bae, *et al.*, Digital Museum of Retinal Ganglion Cells with Dense Anatomy and Physiology. *Cell* **173**, 1293-1306.e19 (2018).

5. W. Huang, *et al.*, Linking transcriptomes with morphological and functional phenotypes in mammalian retinal ganglion cells. *Cell Rep.* **40**, 111322 (2022).
6. B. A. Rheaume, *et al.*, Single cell transcriptome profiling of retinal ganglion cells identifies cellular subtypes. *Nat. Commun.* **9**, 2759 (2018).
7. N. M. Tran, *et al.*, Single-Cell Profiles of Retinal Ganglion Cells Differing in Resilience to Injury Reveal Neuroprotective Genes. *Neuron* **104**, 1039-1055.e12 (2019).
8. J. R. Sanes, R. H. Masland, The Types of Retinal Ganglion Cells: Current Status and Implications for Neuronal Classification. *Annu. Rev. Neurosci.* **38**, 221–246 (2015).
9. D. Kerschensteiner, Feature Detection by Retinal Ganglion Cells. *Annu. Rev. Vis. Sci.* **8**, 135–169 (2022).
10. F. Marcucci, C. A. Soares, C. Mason, Distinct timing of neurogenesis of ipsilateral and contralateral retinal ganglion cells. *J. Comp. Neurol.* **527**, 212–224 (2019).
11. U. C. Dräger, Birth dates of retinal ganglion cells giving rise to the crossed and uncrossed optic projections in the mouse. *Proc. R. Soc. Lond. B Biol. Sci.* **224**, 57–77 (1985).
12. M. H. Farah, S. S. Easter, Cell birth and death in the mouse retinal ganglion cell layer. *J. Comp. Neurol.* **489**, 120–134 (2005).
13. L. Galli, L. Maffei, Spontaneous impulse activity of rat retinal ganglion cells in prenatal life. *Science* **242**, 90–91 (1988).
14. M. Meister, R. O. L. Wong, D. A. Baylor, C. J. Shatz, Synchronous Bursts of Action Potentials in Ganglion Cells of the Developing Mammalian Retina. *Science* **252**, 939–943 (1991).
15. R. O. L. Wong, RETINAL WAVES AND VISUAL SYSTEM DEVELOPMENT. *Annu. Rev. Neurosci.* **22**, 29–47 (1999).
16. A. G. Blankenship, M. B. Feller, Mechanisms underlying spontaneous patterned activity in developing neural circuits. *Nat. Rev. Neurosci.* **11**, 18–29 (2010).
17. M. B. Feller, D. P. Wellis, D. Stellwagen, F. S. Werblin, C. J. Shatz, Requirement for Cholinergic Synaptic Transmission in the Propagation of Spontaneous Retinal Waves. *Science* **272**, 1182–1187 (1996).
18. C. Voufo, *et al.*, Circuit mechanisms underlying embryonic retinal waves. *eLife* **12**, e81983 (2023).
19. Z. J. Zhou, Direct Participation of Starburst Amacrine Cells in Spontaneous Rhythmic Activities in the Developing Mammalian Retina. *J. Neurosci.* **18**, 4155–4165 (1998).
20. D. Kerschensteiner, Glutamatergic Retinal Waves. *Front. Neural Circuits* **10** (2016).
21. M. S. Grubb, F. M. Rossi, J.-P. Changeux, I. D. Thompson, Abnormal Functional Organization in the Dorsal Lateral Geniculate Nucleus of Mice Lacking the β2 Subunit of the Nicotinic Acetylcholine Receptor. *Neuron* **40**, 1161–1172 (2003).
22. Y. Murata, M. T. Colonnese, An excitatory cortical feedback loop gates retinal wave transmission in rodent thalamus. *eLife* **5**, e18816 (2016).
23. J. B. Ackman, T. J. Burbridge, M. C. Crair, Retinal waves coordinate patterned activity throughout the developing visual system. *Nature* **490**, 219–225 (2012).
24. T. J. Burbridge, *et al.*, Disruption of Cholinergic Retinal Waves Alters Visual Cortex Development and Function. [Preprint] (2024). Available at: http://biorxiv.org/lookup/doi/10.1101/2024.04.05.588143 [Accessed 11 November 2024].
25. B. J. Choi, Y.-C. D. Chen, C. Desplan, Building a circuit through correlated spontaneous neuronal activity in the developing vertebrate and invertebrate visual systems. *Genes Dev.* **35**, 677–691 (2021).
26. F. J. Martini, T. Guillamón-Vivancos, V. Moreno-Juan, M. Valdeolmillos, G. López-Bendito, Spontaneous activity in developing thalamic and cortical sensory networks. *Neuron* **109**, 2519–2534 (2021).
27. N. Matsumoto, D. Barson, L. Liang, M. C. Crair, Hebbian instruction of axonal connectivity by endogenous correlated spontaneous activity. *Science* **385**, eadh7814 (2024).

28. S. Negueruela, *et al.*, Proper Frequency of Perinatal Retinal Waves Is Essential for the Precise Wiring of Visual Axons in Nonimage-Forming Nuclei. *J. Neurosci.* **44**, e1408232024 (2024).
29. T. A. Seabrook, T. J. Burbridge, M. C. Crair, A. D. Huberman, Architecture, Function, and Assembly of the Mouse Visual System. *Annu. Rev. Neurosci.* **40**, 499–538 (2017).
30. D. Kerschensteiner, M. B. Feller, Mapping the Retina onto the Brain. *Cold Spring Harb. Perspect. Biol.* **16**, a041512 (2024).
31. X. Ge, *et al.*, Retinal waves prime visual motion detection by simulating future optic flow. *Science* **373**, eabd0830 (2021).
32. A. Bansal, *et al.*, Mice Lacking Specific Nicotinic Acetylcholine Receptor Subunits Exhibit Dramatically Altered Spontaneous Activity Patterns and Reveal a Limited Role for Retinal Waves in Forming ON and OFF Circuits in the Inner Retina. *J. Neurosci.* **20**, 7672–7681 (2000).
33. V. Mehta, E. Sernagor, Early neural activity and dendritic growth in turtle retinal ganglion cells. *Eur. J. Neurosci.* **24**, 773–786 (2006).
34. E. Sernagor, N. M. Grzywacz, Influence of spontaneous activity and visual experience on developing retinal receptive fields. *Curr. Biol.* **6**, 1503–1508 (1996).
35. W. T. Wong, R. O. L. Wong, Changing specificity of neurotransmitter regulation of rapid dendritic remodeling during synaptogenesis. *Nat. Neurosci.* **4**, 351–352 (2001).
36. H. Xu, *et al.*, The Immune Protein CD3ζ Is Required for Normal Development of Neural Circuits in the Retina. *Neuron* **65**, 503–515 (2010).
37. A. Tiriac, K. Bistrong, M. N. Pitcher, J. M. Tworig, M. B. Feller, The influence of spontaneous and visual activity on the development of direction selectivity maps in mouse retina. *Cell Rep.* **38**, 110225 (2022).
38. T. J. Burbridge, *et al.*, Visual Circuit Development Requires Patterned Activity Mediated by Retinal Acetylcholine Receptors. *Neuron* **84**, 1049–1064 (2014).
39. F. M. Rossi, *et al.*, Requirement of the nicotinic acetylcholine receptor β2 subunit for the anatomical and functional development of the visual system. *Proc. Natl. Acad. Sci.* **98**, 6453–6458 (2001).
40. K. Shekhar, I. E. Whitney, S. Butrus, Y.-R. Peng, J. R. Sanes, Diversification of multipotential postmitotic mouse retinal ganglion cell precursors into discrete types. *eLife* **11**, e73809 (2022).
41. B. Krieger, M. Qiao, D. L. Rousso, J. R. Sanes, M. Meister, Four alpha ganglion cell types in mouse retina: Function, structure, and molecular signatures. *PLOS ONE* **12**, e0180091 (2017).
42. D. L. Rousso, *et al.*, Two Pairs of ON and OFF Retinal Ganglion Cells Are Defined by Intersectional Patterns of Transcription Factor Expression. *Cell Rep.* **15**, 1930–1944 (2016).
43. I. E. Whitney, *et al.*, Vision-Dependent and -Independent Molecular Maturation of Mouse Retinal Ganglion Cells. *Neuroscience* **508**, 153–173 (2023).
44. E. Z. Macosko, *et al.*, Highly Parallel Genome-wide Expression Profiling of Individual Cells Using Nanoliter Droplets. *Cell* **161**, 1202–1214 (2015).
45. M. Ashburner, *et al.*, Gene Ontology: tool for the unification of biology. *Nat. Genet.* **25**, 25–29 (2000).
46. The Gene Ontology Consortium, *et al.*, The Gene Ontology knowledgebase in 2023. *GENETICS* **224**, iyad031 (2023).
47. P. D. Thomas, *et al.*, PANTHER : Making genome-scale phylogenetics accessible to all. *Protein Sci.* **31**, 8–22 (2022).
48. C. W. Oyster, H. B. Barlow, Direction-Selective Units in Rabbit Retina: Distribution of Preferred Directions. *Science* **155**, 841–842 (1967).
49. J. Elstrott, *et al.*, Direction Selectivity in the Retina Is Established Independent of Visual

Experience and Cholinergic Retinal Waves. *Neuron* **58**, 499–506 (2008).
50. W. Sun, Q. Deng, W. R. Levick, S. He, ON direction-selective ganglion cells in the mouse retina. *J. Physiol.* **576**, 197–202 (2006).
51. O. S. Dhande, *et al.*, Genetic Dissection of Retinal Inputs to Brainstem Nuclei Controlling Image Stabilization. *J. Neurosci.* **33**, 17797–17813 (2013).
52. K. Yonehara, *et al.*, Identification of Retinal Ganglion Cells and Their Projections Involved in Central Transmission of Information about Upward and Downward Image Motion. *PLoS ONE* **4**, e4320 (2009).
53. K. Toma, *et al.*, Perivascular neurons instruct 3D vascular lattice formation via neurovascular contact. *Cell* **187**, 2767-2784.e23 (2024).
54. A. Y. M. Wang, *et al.*, An ON-type direction-selective ganglion cell in primate retina. *Nature* **623**, 381–386 (2023).
55. J. Hahn, *et al.*, Evolution of neuronal cell classes and types in the vertebrate retina. *Nature* **624**, 415–424 (2023).
56. T. Al-Khindi, *et al.*, The transcription factor Tbx5 regulates direction-selective retinal ganglion cell development and image stabilization. *Curr. Biol.* **32**, 4286-4298.e5 (2022).
57. X. Wen, *et al.*, Tandem pore domain acid-sensitive K channel 3 (TASK-3) regulates visual sensitivity in healthy and aging retina. *Sci. Adv.* **8**, eabn8785 (2022).
58. L. C. Greig, M. B. Woodworth, M. J. Galazo, H. Padmanabhan, J. D. Macklis, Molecular logic of neocortical projection neuron specification, development and diversity. *Nat. Rev. Neurosci.* **14**, 755–769 (2013).
59. L. N. Borodinsky, *et al.*, Activity-dependent homeostatic specification of transmitter expression in embryonic neurons. *Nature* **429**, 523–530 (2004).
60. K. W. Marek, L. M. Kurtz, N. C. Spitzer, cJun integrates calcium activity and tlx3 expression to regulate neurotransmitter specification. *Nat. Neurosci.* **13**, 944–950 (2010).
61. A. Nakashima, *et al.*, Structured spike series specify gene expression patterns for olfactory circuit formation. *Science* **365**, eaaw5030 (2019).
62. C. R. Yu, *et al.*, Spontaneous Neural Activity Is Required for the Establishment and Maintenance of the Olfactory Sensory Map. *Neuron* **42**, 553–566 (2004).
63. A. S. Mobley, *et al.*, Hyperpolarization-Activated Cyclic Nucleotide-Gated Channels in Olfactory Sensory Neurons Regulate Axon Extension and Glomerular Formation. *J. Neurosci.* **30**, 16498–16508 (2010).
64. S. Serizawa, *et al.*, A Neuronal Identity Code for the Odorant Receptor-Specific and Activity-Dependent Axon Sorting. *Cell* **127**, 1057–1069 (2006).
65. E. O. Williams, *et al.*, Delta Protocadherin 10 is Regulated by Activity in the Mouse Main Olfactory System. *Front. Neural Circuits* **5** (2011).
66. S. Sun, *et al.*, Hair Cell Mechanotransduction Regulates Spontaneous Activity and Spiral Ganglion Subtype Specification in the Auditory System. *Cell* **174**, 1247-1263.e15 (2018).
67. B. R. Shrestha, *et al.*, Sensory Neuron Diversity in the Inner Ear Is Shaped by Activity. *Cell* **174**, 1229-1246.e17 (2018).
68. P. Bastien-Dionne, L. S. David, A. Parent, A. Saghatelyan, Role of sensory activity on chemospecific populations of interneurons in the adult olfactory bulb. *J. Comp. Neurol.* **518**, 1847–1861 (2010).
69. B. Tepe, *et al.*, Single-Cell RNA-Seq of Mouse Olfactory Bulb Reveals Cellular Heterogeneity and Activity-Dependent Molecular Census of Adult-Born Neurons. *Cell Rep.* **25**, 2689-2703.e3 (2018).
70. S. Cheng, *et al.*, Vision-dependent specification of cell types and function in the developing cortex. *Cell* **185**, 311-327.e24 (2022).
71. T. Guillamón-Vivancos, *et al.*, Input-dependent segregation of visual and somatosensory circuits in the mouse superior colliculus. *Science* **377**, 845–850 (2022).
72. L. Wang, *et al.*, Direction-Specific Disruption of Subcortical Visual Behavior and Receptive

Fields in Mice Lacking the β2 Subunit of Nicotinic Acetylcholine Receptor. *J. Neurosci.* **29**, 12909–12918 (2009).
73. K. L. Briggman, M. Helmstaedter, W. Denk, Wiring specificity in the direction-selectivity circuit of the retina. *Nature* **471**, 183–188 (2011).
74. A. S. Mauss, A. Vlasits, A. Borst, M. Feller, Visual Circuits for Direction Selectivity. *Annu. Rev. Neurosci.* **40**, 211–230 (2017).
75. R. D. Morrie, M. B. Feller, An Asymmetric Increase in Inhibitory Synapse Number Underlies the Development of a Direction Selective Circuit in the Retina. *J. Neurosci.* **35**, 9281–9286 (2015).
76. J. Tworig, *et al.*, Differential expression analysis identifies candidate synaptogenic molecules for wiring direction-selective circuits in the retina. *J. Neurosci.* e1461232024 (2024). https://doi.org/10.1523/JNEUROSCI.1461-23.2024.
77. W. Wei, M. B. Feller, Organization and development of direction-selective circuits in the retina. *Trends Neurosci.* **34**, 638–645 (2011).
78. K. Yonehara, *et al.*, Spatially asymmetric reorganization of inhibition establishes a motion-sensitive circuit. *Nature* **469**, 407–410 (2011).
79. 10X Genomics, What fraction of mRNA transcripts are captured per cell? *10X Genomics*. Available at: https://kb.10xgenomics.com/hc/en-us/articles/360001539051-What-fraction-of-mRNA-transcripts-are-captured-per-cell [Accessed 2 December 2024].
80. A. E. West, M. E. Greenberg, Neuronal Activity-Regulated Gene Transcription in Synapse Development and Cognitive Function. *Cold Spring Harb. Perspect. Biol.* **3**, a005744–a005744 (2011).
81. M. Dziembowska, *et al.*, Activity-Dependent Local Translation of Matrix Metalloproteinase-9. *J. Neurosci.* **32**, 14538–14547 (2012).
82. S. A. Shuster, *et al.*, In situ cell-type-specific cell-surface proteomic profiling in mice. *Neuron* **110**, 3882-3896.e9 (2022).
83. M. Van Oostrum, *et al.*, The proteomic landscape of synaptic diversity across brain regions and cell types. *Cell* **186**, 5411-5427.e23 (2023).
84. W. Xu, *et al.*, Multiorgan Autonomic Dysfunction in Mice Lacking the β2 and the β4 Subunits of Neuronal Nicotinic Acetylcholine Receptors. *J. Neurosci.* **19**, 9298–9305 (1999).
85. M. Pachitariu, C. Stringer, Cellpose 2.0: how to train your own model. *Nat. Methods* **19**, 1634–1641 (2022).
86. C. Stringer, T. Wang, M. Michaelos, M. Pachitariu, Cellpose: a generalist algorithm for cellular segmentation. *Nat. Methods* **18**, 100–106 (2021).
87. A. Imbert, *et al.*, FISH-quant v2: a scalable and modular tool for smFISH image analysis. *RNA* **28**, 786–795 (2022).
88. N. Otsu, A Threshold Selection Method from Gray-Level Histograms. *IEEE Trans. Syst. Man Cybern.* **9**, 62–66 (1979).
89. F. A. Wolf, P. Angerer, F. J. Theis, SCANPY: large-scale single-cell gene expression data analysis. *Genome Biol.* **19**, 15 (2018).
90. R. Satija, J. A. Farrell, D. Gennert, A. F. Schier, A. Regev, Spatial reconstruction of single-cell gene expression data. *Nat. Biotechnol.* **33**, 495–502 (2015).
91. I. Korsunsky, *et al.*, Fast, sensitive and accurate integration of single-cell data with Harmony. *Nat. Methods* **16**, 1289–1296 (2019).
92. V. A. Traag, L. Waltman, N. J. Van Eck, From Louvain to Leiden: guaranteeing well-connected communities. *Sci. Rep.* **9**, 5233 (2019).
93. L. McInnes, J. Healy, J. Melville, UMAP: Uniform Manifold Approximation and Projection for Dimension Reduction. [Preprint] (2020). Available at: http://arxiv.org/abs/1802.03426 [Accessed 24 October 2024].

94. T. Chen, C. Guestrin, XGBoost: A Scalable Tree Boosting System in *Proceedings of the 22nd ACM SIGKDD International Conference on Knowledge Discovery and Data Mining*, (2016), pp. 785–794.

Methods

Mice

All procedures were approved by University of California, Berkeley Institutional Animal Care and Use committee and were in accordance with the National Institutes of Health Guide for the Care and Use of Laboratory Animals, the Public Health Service Policy, and the Society for Neuroscience Policy on the Use of Animals in Neuroscience Research. Mice used in this study were P7-P60 and of both sexes. Our control experiments were performed using C57BL/6J (RRID:IMSR_JAX:000664). β2KO mice that were deficient in the beta-2 subunit of the nicotinic acetylcholine receptor were originally provided by Dr. Art Beaudet from Baylor College of Medicine (84) and maintained in our laboratory onto a C57BL/6J background. Genotyping was performed by Transnetyx.

RGC isolation

P7 C57BL/6J and β2KO mice were anesthetized in an isoflurane induction chamber and euthanized by decapitation. All the solutions were filtered using 0.22 µm syringe filter (Fisher #9720511). Eyes were enucleated and retinas were immediately dissected in oxygenated (95% oxygen/5% carbon dioxide) Ames' media with L-glutamine and sodium bicarbonate (pH ~7.4) at room temperature under light scope. Retinas (6 to 8 per sample) were digested for 10 min at 37ºC in 70 µl papain (Fisher #LS003126) + 50 µl DNase (Sigma #D4527-40KU) + 50 µl L-cysteine (Sigma #C1276-10G) in 5 ml Ames, which was activated at 37ºC for 15 min. Samples were gently swirled once during this incubation. Following this, papain was removed and samples was gently triturated with P1000 pipette tips in 1 ml 10x ovomucoid (Fisher #NC9931428) + 50 µl DNase + 9 ml Ames. Manual trituration was performed using 2 ml of ovo solution at a time and the supernatant was filtered using 40 µm cell strainer in a new tube. This cell suspension was spun down at 450 *g* for 8 min. Supernatant was discarded and the pellet was resuspended in 250 µl of Ames + bovine serum albumin (BSA). This solution was prepared using 27 ml Ames + 3 ml 4% BSA (Sigma #A9418-5G) + 50 µl DNase. Cells were counted using hemocytometer (1:100 dilution factor with trypan blue). 10 million cells were incubated in 10 µl CD90.2 microbeads (Miltenyi Biotec #130-121-278) for 10 min at 4ºC. Following incubation, 6 ml Ames + BSA solution was added and cells were spun down at 450 *g* for 8 min. Supernatant was discarded and cells were resuspended in fresh 500 µl Ames + BSA solution. Cell suspension was subjected to magnetic-activated cell sorting (MACS) using large cell columns (Miltenyi Biotec #130-042-202) to sort RGCs. To obtain a high number of RGCs, the tube containing the cells was washed with 500 µl Ames + BSA solution for 2 times. To obtain better purity, MACS was repeated one more time on eluted $CD90.2^+$ RGCs using fresh columns. This cell suspension was spun down at 450 *g* for 8 min and the supernatant was removed. Pellet obtained was resuspended in ~1000 µl of Ames + BSA and cell concentration was counted using hemocytometer (dilution factor 2). This spun down strategy was employed to obtain a highly concentrated sample in a small volume of ~100 µl Ames + BSA.

10X genomics

Single-cell libraries on RGCs isolated were prepared using Chromium Next GEM Single Cell 3' Kit v3.1 (10X Genomics, Pleasanton, CA) following manufacturer's protocol. On average, for each sample, cells were loaded to ultimately recover 5000-10000 cells. At least 3 biological replicates (each referred to as a sample) were run for each genotype and each sample included RGCs pooled from 3-4 mice. All 10X-related steps were performed by QB3 Genomics of University of California, Berkeley, Berkeley, California, RRID: SCR_022170. Libraries were sequenced on the Illumina NovaSeq platform at the University of California, Irvine Genomics Research & Technology Hub.

In situ RNA hybridization (ISH) and immunohistochemistry (IHC)

Retinas were dissected as described above, fixed in 4% paraformaldehyde overnight at 4ºC, and then submerged in 30% sucrose solution for ~3 days at 4ºC. Using a cryostat, retinas were thinly sliced to a thickness of 16 µm.

RNAscope® Multiplex Fluorescent Detection Kit v2 (ACD #323110) was performed to detect *Kcnk9* mRNA (ACD #475681) using the manufacturer's instructions for fixed frozen tissue. Only few changes were made to their established protocol. These were: incubating tissue in 4% PFA for 1 hr instead of 15 min; 5 min of target retrieval; and protease treatment for only 15 min. Opal dyes (Akoya #FP1487001KT) at 1:750 dilution were used for signal detection. Following ISH, IHC was performed to detect SMI32$^+$ (1:250 dilution, BioLegend #801702,) and RBPMS$^+$ (1:500 dilution, Abcam #ab152101) cells. Blocking solution used was 1% BSA + 0.2% Triton X-100 in 1X Tris-buffered saline (TBS). Retinal slices were blocked for 30 mins at room temperature and incubated in primary antibodies (prepared in blocking solution) overnight at 4ºC. Next day, retinal slices were washed for 3 times (15 min each) in 0.1% Tween 20 and 0.1% Triton X-100 in 1X TBS solution and incubated in secondary antibodies (1:500 dilution prepared in blocking solution, Jackson ImmunoResearch #111-605-003, Fisher #A28175) for 2 hr at room temperature. After a few washes, slides were mounted with media containing DAPI (Fisher #H-1500).

Retinal slices were imaged on a Zeiss LSM880 Laser Scanning Confocal Microscope with a Plan-Apochromat 20x/0.8 M27 objective and resolution of 2048 by 2048 pixel (pixel size: 0.208 µm^2) at Molecular Imaging Center at University of California, Berkeley. Z-stacks with 2 µm were used to acquire images. Representative images in the figures are maximum intensity projections, while colocalization of *Kcnk9* mRNA signal with RBPMS and SMI32 was confirmed using single-plane images.

Quantification and statistical analysis of ISH and IHC signal

RGCs were identified in each image to allow for reporting of per-cell metrics. Cells were segmented on the RBPMS IHC channel using the pretrained Cellpose model cyto3, which was fine-tuned using manually annotated images (85, 86). DAPI stains were also provided to the segmentation model to distinguish proximal cells. RGCs identified through this segmentation that colocalized with SMI32 were labeled as αRGCs.

Quantification of the ISH signal was performed using the Python package Big-FISH (87). Signal was quantified using the number of puncta per cell and average intensity per cell. To

count the number of *Kcnk9* puncta in each cell, the image was first background subtracted using a mean subtraction within a 2-pixel-wide square kernel. A Laplacian of Gaussian filter was then used to denoise the image. Puncta were identified as local maxima in the filtered image. Finally, an intensity threshold determined through Otsu's method was used to filter for high-intensity puncta (88). A mask from the cell segmentation was used to then compute the number of puncta per cell. Average intensity per cell was computed by averaging the intensities of all pixels within a cell in the Cellpose mask.

Significance testing between conditions for both puncta counts and intensities was performed using a Mann-Whitney U-Test, taking each cell as an individual observation.

Patch-clamp electrophysiology of RGCs

Voltage-clamp experiments on αRGCs to identify leak channel-associated conductance were performed as described previously (57). P7-P12 (all before eye opening) C57BL/6J and β2KO mice were anesthetized in an isoflurane induction chamber and euthanized by decapitation. Eyes were enucleated and retinas were immediately dissected at room temperature under light scope in oxygenated (95% oxygen/5% carbon dioxide) Ames' media with L-glutamine and sodium bicarbonate with pH of 7.4, adjusted using NaOH/HCl (~300 mOsm). Isolated retinas were placed flat in the recording chamber with a continuous perfusion of oxygenated Ames at ~2 ml/min. A temperature of 32–34°C was maintained for the duration of experiments. Recordings were performed in light, except when taking morphology images under two-photon illumination.

MultiClamp 700B amplifier, Digidata 1440A digitizer, and pCLAMP 10.7 software were used for patch-clamp experiments. Patch pipettes were pulled from borosilicate glass capillaries (with an outer diameter of 1.5 mm and an inner diameter of 1.1 mm) and resistance of ~5 MΩ (PC-10 pipette puller; Narishige). The internal solution contained (in mM): 125 K-gluconate, 2 $CaCl_2$, 2 $MgCl_2$, 10 EGTA, 10 Hepes, 0.5 Mg–ATP, and 2 Na_2–GTP (~290 mOsm). To fill the cell, 10 μM Alexa Fluor 488 hydrazide (Life Technologies #A10436) was also added to the internal solution. pH of the solution was ~7.2 and adjusted using KOH. The liquid junction potential corrected was -13 mV. αRGCs were identified based on their large soma size and dendritic field, which was identified via the Alexa Fluor 488 dye-filled cell (41). Cells were voltage-clamped at -73 mV for 100 ms, following holding at +17 mV for 500 ms and ramped to -133 mV within 500 ms. In bath solution, tetrodotoxin (TTX, to block voltage-gated sodium channels) at 500 nM and 4-Aminopyridine (4-AP, to block voltage-gated potassium channel) at 5 mM were added to Ames to isolate leak channel-associated conductance.

Current required to hold WT and β2KO RGCs at +17 mV was calculated by subtracting current required to hold at -73 mV from current required to hold at +17 mV during ramp protocol. Statistical analysis was performed using R. Data in the figure 4G is represented as means with standard deviation. Welch two-sample t-test was performed as unequal sample size and without assuming equal variances between the samples. P value less than 0.05 was defined as significant.

Code availability

Jupyter notebooks required to reproduce the analyses presented here are available on our GitHub page: https://github.com/shekharlab/WaveRGCs.

Data availability

All raw and processed scRNAseq datasets reported in this study will be made publicly available via NCBI's Gene Expression Omnibus (GEO) Accession Number GSE283463. Processed h5ad files are available at https://github.com/shekharlab/WaveRGCs. These h5ad files contain all relevant metadata and log-normalized counts.

Alignment and quantification of scRNAseq data

Sequencing read libraries generated in this work (P7 WT and β2KO) were aligned to the UCSC mm10 genome assembly using Cellranger v7.1.0 (10X Genomics). This alignment was performed separately on each sample (three P7 WT samples, four P7 β2KO samples), and the resulting cells-by-genes expression matrices were combined to obtain an expression matrix for each condition.

Preprocessing of expression data was performed using the Scanpy workflow (89). Cells expressing less than 700 genes, containing less than 5,000 transcripts, or with over 10% of its counts from mitochondrial genes were filtered out of the data. The count matrix $\mathbf{X}$ was then normalized such that each column sums to 10,000 (corresponding to total reads per cell) and logarithmized such that, for a normalized matrix entry x_{ij}, its corresponding entry in the log-transformed matrix is $log(x_{ij} + 1)$.

Clustering

Highly variable genes (HVGs) were identified using a previously published method (90) based on the ratio of a gene's expression variance to its mean. Briefly, the column mean (μ_j) and variance (σ_j^2) of $\mathbf{X}$ were computed and used to calculate a dispersion metric

$$D = \frac{\sigma_j^2}{\mu_j}$$

which was used to split all genes into twenty bins. Within each bin, dispersion metrics were z-scored, and those genes with a z-score greater than 2 were identified as highly variable. The expression matrix was then subset to HVGs and scaled along columns (genes) to unit variance and zero mean. Principal components analysis (PCA) was applied to reduce the dimensionality of the data, then batch correction was applied via Harmony (91). The top 30 batch-corrected PCs were used to build a k-nearest neighbors graph, which was used to cluster cells via the Leiden algorithm (92) and create a Uniform Manifold Approximation and Projection (UMAP) embedding of cells for visualization (93). We emphasize that UMAP was used only for the post hoc visualization of clusters, and was not used to guide the graph construction or clustering procedure.

Type identification

P7 WT and β2KO clusters were assigned to classes based on expression of known retinal cell class markers. Clusters expressing *Slc17a6*, *Rbpms*, *Pou4f1*, *Pou4f2*, and *Pou4f3* were identified as RGCs and separated from the other classes for further analysis. RGCs were then annotated with adult type labels via a supervised classification approach using gradient

boosted trees (XGBoost) (94). In this approach, a classifier learns the transcriptomic signatures of cell types from a reference dataset (e.g. P56 cell types) to then assign type labels to cells in a test dataset (e.g. P7 cells). Details of the implementation can be found in (40). Briefly, two classifiers are trained on the reference (from which labels are learned) and test (to which labels are applied) datasets independently to identify features that contribute the highest average information gain across decision trees. Then, the top 500 discriminatory features are used in the training of a third classifier on the reference dataset. This classifier is then used to assign labels to cells in the test dataset. The classifier assigns a vector of probabilities to each cell, where entry p_i of the vector corresponds with the probability that the cell belongs to label i. The label i that maximizes p_i is then chosen as the label for the cell, unless the maximal p_i is less than a threshold of 0.05. The same label transfer method was used to assign P56 types to P5 cells. XGBoost was run using a multi-log loss function and hyperparameter values `eta = 0.6`, `max_depth = 6`, and `subsample = 0.6`.

Analysis of wave-dependent changes in gene expression

For all genes included in the four datasets, log2-fold changes were calculated for each pair of datasets. In the assessment of global gene expression changes, expression values were averaged over all cells in each dataset. For a gene g with average normalized expression x_{gi} at condition i, the log2-fold change between conditions a and b was calculated as $log_2\left(\frac{x_{ga}+\epsilon}{x_{gb}+\epsilon}\right)$, where $\epsilon = 0.01$ is a small pseudocount used to avoid undefined or extreme values. The same calculation was done to find inter-replicate log2-fold changes.

To assess type-specific gene expression changes, a similar calculation was done with average gene expression values representing type-condition pair averages rather than condition averages. Additionally, a larger pseudocount was used to account for the smaller quantity of cells within each type. That is, for a gene g with average normalized expression x_{gij} at condition i in type j, the log2-fold change between conditions a and b in type t was calculated as $log_2\left(\frac{x_{gat}+\epsilon}{x_{gbt}+\epsilon}\right)$, where $\epsilon = 0.1$.

To investigate wave-dependent, type-specific changes in expression, we focused on changes between P7 WT and β2KO. For each type, a differential expression test (Wilcoxon rank-sum) was performed on the set of genes with a log2-fold change of at least 1.2 in magnitude. Genes with an adjusted p-value of at most 0.05 were then selected for Gene Ontology (GO) analysis.

Statistical overrepresentation analysis was performed using the PANTHER web interface (45–47) to identify GO terms associated with each set of wave-regulated genes. The test utilizes an input test set and background set to assign a p-value to each GO term. For a given GO term, let k represent the number of genes in the test set belonging to the GO term, n the length of the full test set, K the number of genes in the background set belonging to the GO term, and N the length of the full background set. Then, the probability that the term is enriched in the test set is calculated as

$$p = \sum_{i=k}^{K} \frac{\binom{K}{i}\binom{N-K}{n-i}}{\binom{N}{n}}.$$

Two tests were performed to assess the GO terms enriched in both the β2KO upregulated and downregulated gene sets. For each of these tests, the test set was the set of genes that was found to be significantly upregulated or downregulated in P7 β2KO compared to P7 WT, and the input background set was the set of genes that passed the log2-fold change threshold. From this test, we identified those GO terms with adjusted p-values less than 0.1 and selected a few that are relevant to neuronal circuit development to highlight.

A

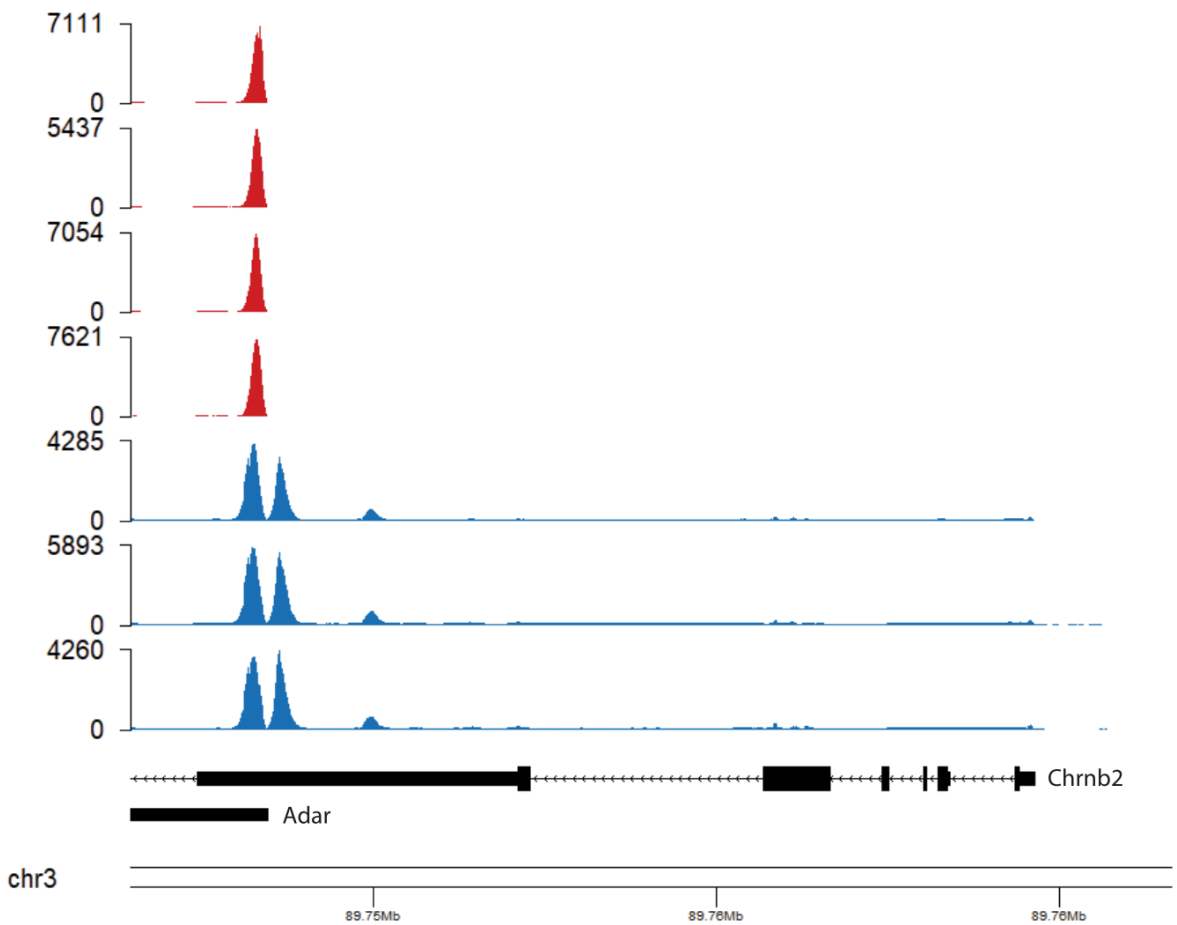

Figure S1. Reads from each sample mapped to the genome. The three WT samples are shown in blue (bottom), and the four β2KO samples are shown in red (top). A negligible amount of reads from the β2KO map to *Chrnb2*, and expression of the gene is likely due to reads from *Adar* mapping onto *Chrnb2*.

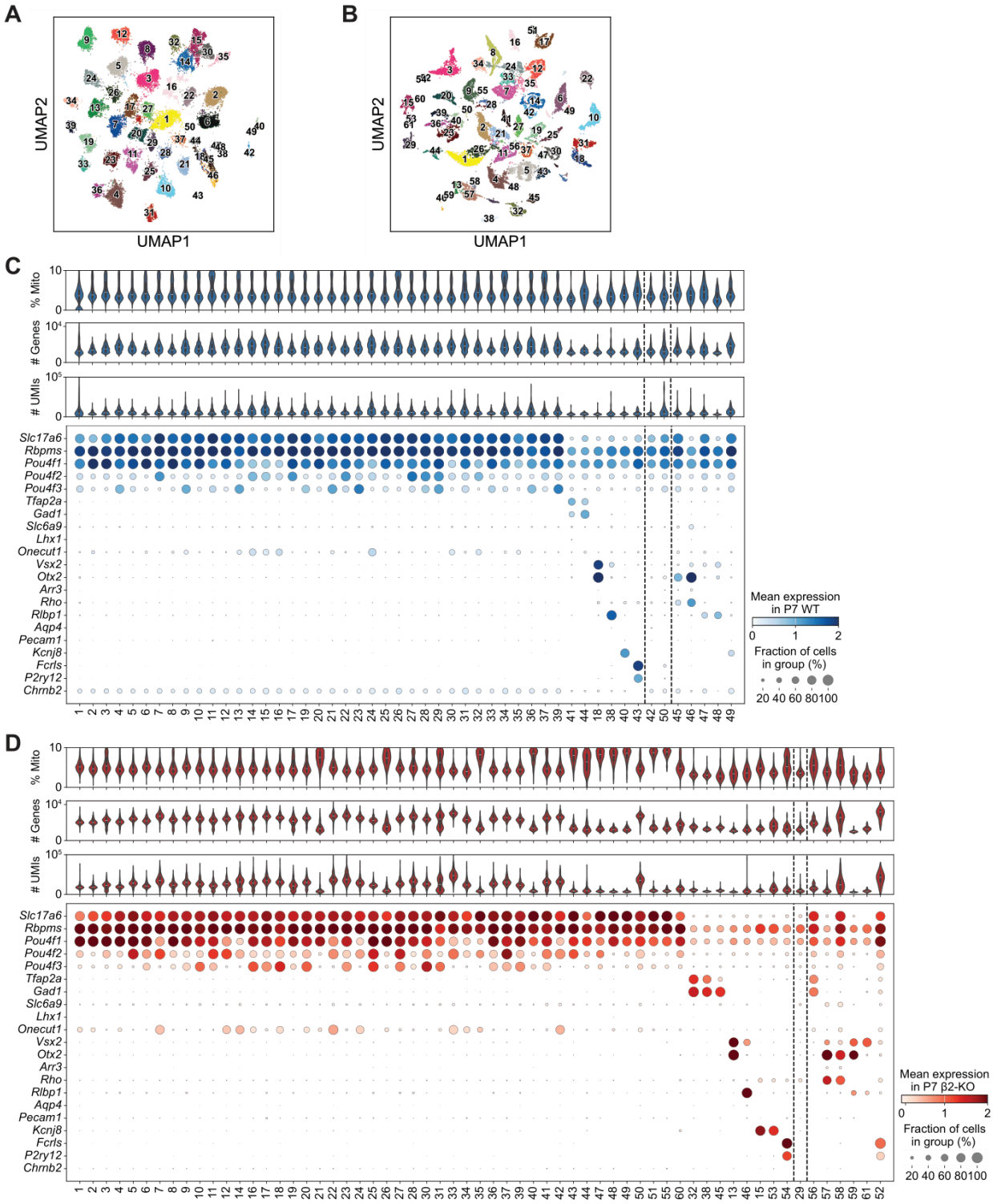

Figure S2. Classification and filtering of P7 cells. **(A-B)** UMAP representations of **(A)** P7 WT and **(B)** P7 β2KO cells colored by clusters assigned via the Leiden algorithm. **(C)** Cell quality metrics and expression profiles for P7 WT clusters. From top to bottom: mitochondrial proportion of genes per cell, number of genes expressed per cell, number of unique molecular identifiers

(UMIs) per cell, and cluster expression of retinal cell class markers. Dotted lines separate clusters with clear class marker expression (left) from those expressing no retinal class markers (middle) and those expressing more than one class marker (right). **(D)** Same as (C) for P7 β2KO clusters.

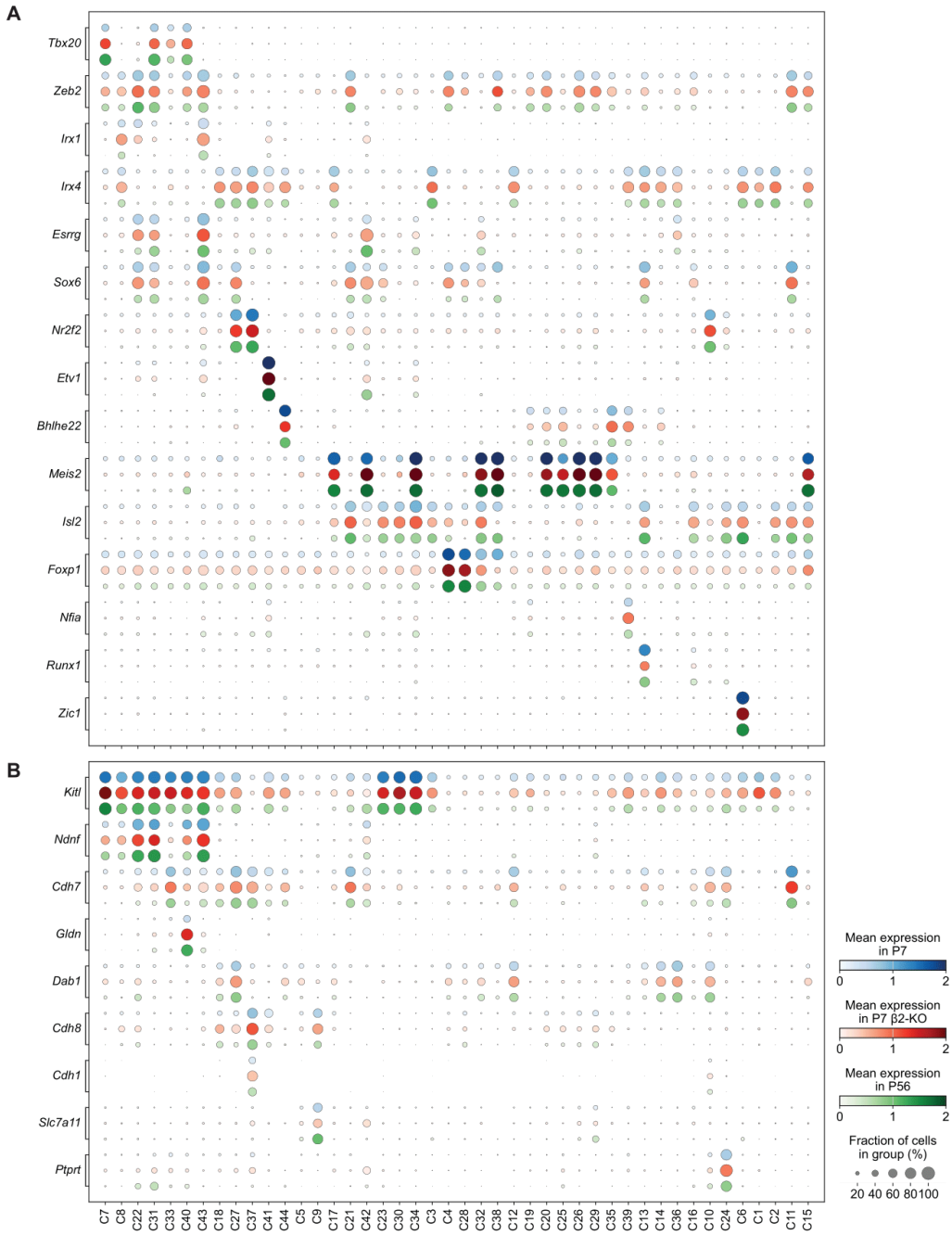

Figure S3. Congruent cell type-specific expression profiles of P7 WT, P7 β2KO, and P56 WT cells. Expression of (A) transcription factors and (B) cell adhesion molecules that are selectively expressed across RGC types.

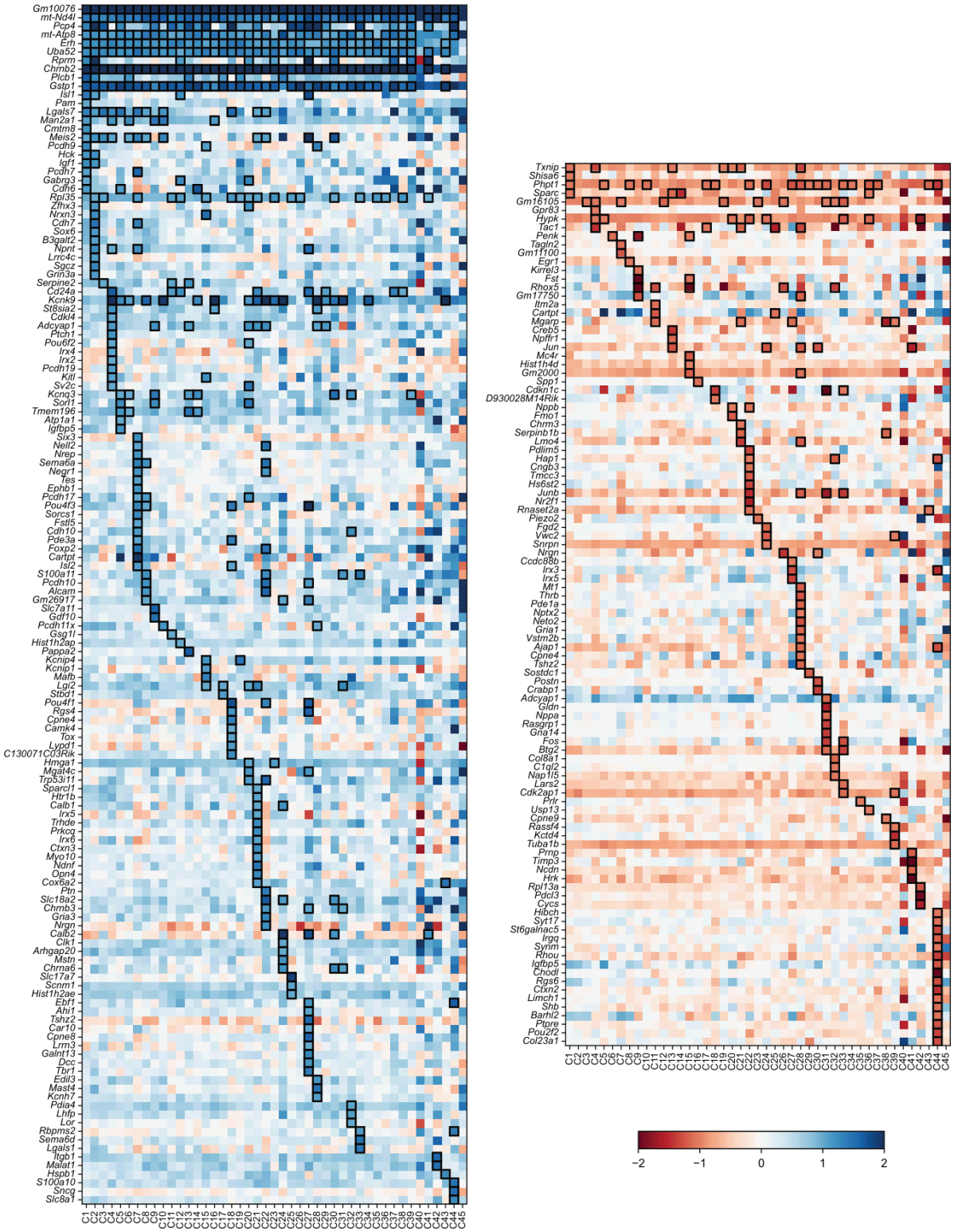

Figure S4. P7 WT vs. β2KO log2FC in all genes found to be significantly up/downregulated in at least one type. Black boxes indicate significant up/downregulation of a gene in a RGC type.

(log2-FC > 1, Wilcoxon rank-sum test adjusted p-value < 0.05). Blue corresponds to higher expression in WT and red corresponds to higher expression in β2KO.

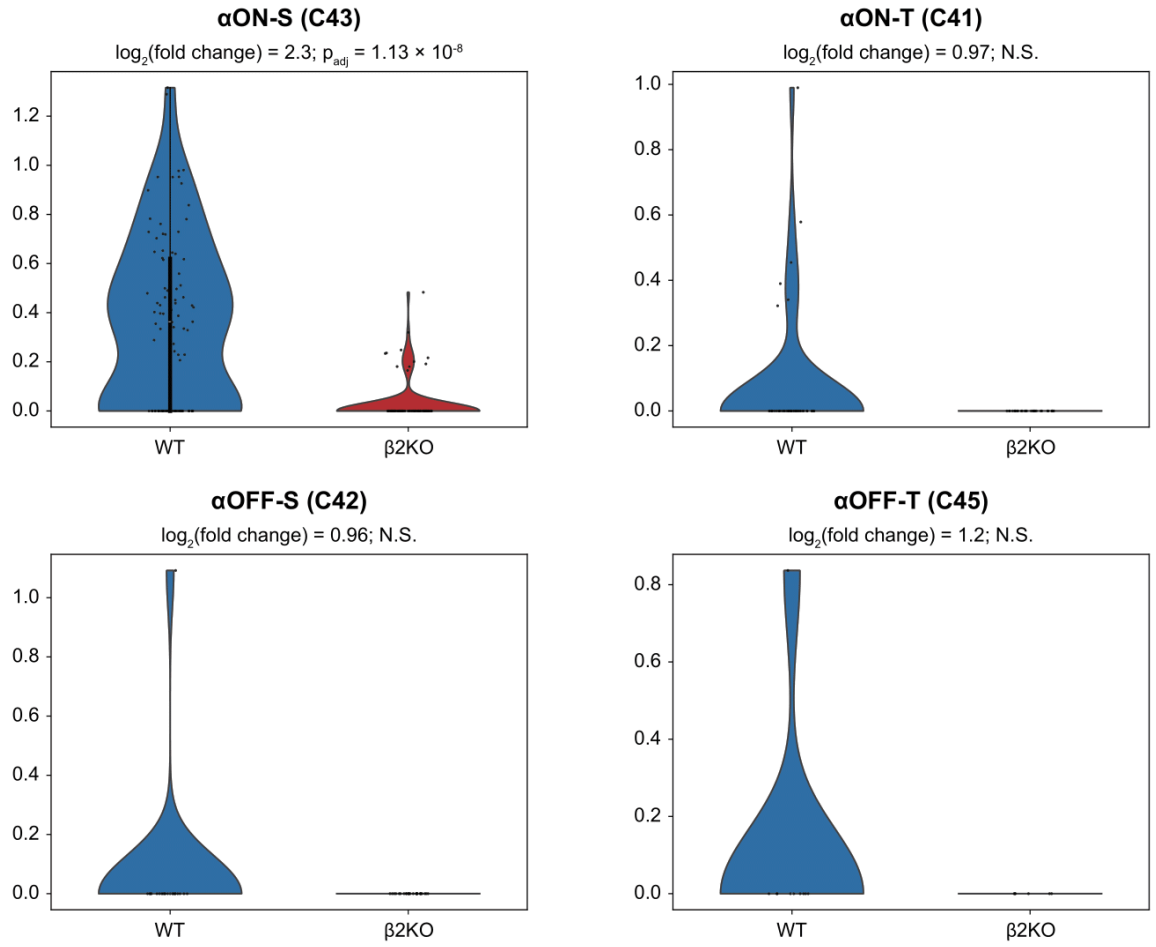

Figure S5. Downregulation of *Kcnk9* in αRGCs. Average expression of *Kcnk9* is higher in the WT condition for all αRGC types, but this difference is only found to be significant (Wilcoxon rank-sum test adjusted p-value < 0.05) in αON-S RGCs due to low sampling of αRGCs. Note that fold changes are calculated using a pseudocount to avoid division by zero (**Methods**).

Table S1. Common names associated with type IDs. Adapted from (7) with mapping information from (3) and morphology information from (5).

Type ID	Subclass	Common Name	Mapping	Morphology
C12	ON-OFF DSGCs	N-ON-OFF DSGC		37*
C16		D/V ON-OFF DSGC (split in **Fig. 4**)	ooDS D	37*
C24		T-ON-OFF DSGC	onDS V, onDS N, onDS T	37*
C10	ON DSGCs	D/V/N-ON DSGC (split in **Fig. 4**)	ooDS T	7i/7o
C1	W3-RGCs	W3L1		
C13		W3L2	HD 1	
C2		W3D1	W3D1	
C6		W3B	HD2	
C23		W3D2		
C30		W3D3	ON tr SmRF	6sn
C3	Foxp2-RGCs	F-mini-ON	F-mini-on	
C4		F-mini-OFF		
C28		F-midi-OFF		2aw
C38		F-midi-ON	ONvOS SmRF	6t
C32		F-Novel		82n
C5	Tbr1-RGCs	J-RGC	OFFvOS	2aw
C17		Tbr1-S1		
C21		Tbr1-S2	Off trSmRF	4i
C9		Tbr1-Novel	OFFhOS	2aw
C42	αRGCs	αOFF-S		1wt, 1ni
C45		αOFF-T	OFF tra alpha	4ow
C41		αON-T		
C43		αON-S/M4	ON alpha	8w
C31	ipRGCs	M2		
C33		M1a	M1	
C40		M1b		
C22		MX		
C7	Novel_Eomes	Novel_7		82wi, 8n
C8		Novel_8		
C19	Novel_Neurod2	Novel_19		
C20		Novel_20		
C25		Novel_25	bSbC	37*, 73
C26		Novel_26	sSbC EW27	27
C29		Novel_29		5so
C35		Novel_35		
C39		Novel_39		5si
C11	Other	Novel_11	LED	5so
C14		Novel_14	ON delayed	37*, 73
C15		Novel_15		
C18		Novel_18	ON bursty	73
C27		Novel_27	ONhOS SmRF	7i/7o
C34		Novel_34		6sn
C36		Novel_36	ONhOS LgRF	8n, 82wo
C37		Novel_37		27
C44		Novel_44		8n